Journal of Aerosol Science 151 (2021) 105672

Contents lists available at ScienceDirect

Journal of Aerosol Science

journal homepage: http://www.elsevier.com/locate/jaerosci

Tutorial: Understanding the transport, deposition, and translocation of particles in human respiratory systems using Computational Fluid-Particle Dynamics and Physiologically Based Toxicokinetic models

Yu Feng *, Jianan Zhao, Hamideh Hayati, Ted Sperry, Hang Yi

School of Chemical Engineering, Oklahoma State University, Stillwater, OK, 74078, USA

ARTICLE INFO

Keywords:
Computational fluid-particle dynamics (CFPD)
Physiologically based pharmacokinetic/ toxicokinetic (PBPK/TK) model
Virtual human
The next-generation lung model

ABSTRACT

Dynamic modeling of how particulate matter (PM) transport, deposit, and translocate from human respiratory systems to systemic regions subject to indoor and outdoor exposures are essential for case-specific lung dosimetry predictions and occupational health risk assessments. Because of the invasive nature and imaging resolution limitations of existing *in vitro* and *in vivo* methods, Computational Fluid-Particle Dynamics plus Physiologically Based Pharmacokinetic/ Toxicokinetic (CFPD-PBPK/TK) models have been employed to predict the fate of the respirable aerosols for decades. This paper presents a guide on how to use the multiscale CFPD-PBPK/TK models to predict lung dosimetry and systemic translocations quantitatively with 3D subject-specific human respiratory systems. The tutorial aims to clarify possibly ambiguous concepts. The step-by-step modeling procedure should help researchers set up the CFPD-PBPK/TK model accurately, following the standard model validation and verification (V&V) processes, and to bring the lung dosimetry predictions to health endpoints. Starting from the fundamentals of CFPD and PBPK/TK governing equations, the tutorial covers the problem identification, pre-processing, solving, and post-processing steps to perform a computational lung aerosol dynamics simulations, emphasizing on (a) the importance of correct reconstruction and mesh generation of the pulmonary airways; (b) the significance of choosing the appropriate turbulence model to predict the laminar-to-turbulence pulmonary airflow regimes; and (c) the standard (V&V) procedures of submodels in the CFPD-PBPK/TK modeling framework. The tutorial also highlights the deficiencies of current CFPD-PBPK/TK models, clarifies the missing biomechanisms and aerosol dynamics in the respiratory systems that need to be considered to build the next-generation virtual human whole-lung models.

1. Introduction

Airborne particulate matter (PM), especially the inhalable particles or droplets with diameters less than 2.5 μm ($PM_{2.5}$) have been a health concern for many decades (Chuang, 2019). Specifically, exposures to fine and ultrafine PM may have adversely affected human health, causing respiratory diseases, neurological ailments, and ultimately cancer (Bakand & Hayes, 2016; Chuang, 2019). It is widely

* Corresponding author. School of Chemical Engineering, Oklahoma State University, 420 Engineering North, Stillwater, OK, 74078.
E-mail address: yu.feng@okstate.edu (Y. Feng).

https://doi.org/10.1016/j.jaerosci.2020.105672
Received 26 June 2020; Received in revised form 10 September 2020; Accepted 13 September 2020
Available online 1 October 2020
0021-8502/

accepted that the respiratory pathological responses to the inhaled PM in humans and mammals are mainly induced by their deposition and retention in the airway. An association has been demonstrated between inhaled ultrafine particles and various adverse health effects, including increased morbidity and mortality (Bakand & Hayes, 2016). Inhaled nanoparticle deposition in lung airways is more uniformly distributed in human lung airways compared to microparticles (Feng et al., 2018). Due to their small size, nanoparticles can cross biological barriers, such as the air-blood barrier, and therefore can reach cells and tissues normally protected (Som, Wick, Krug, & Nowack, 2011).

Although measurements have been done on particle deposition in human patient tissues as well as *in vivo* animal studies, there are many ethical constraints that significantly limit the operational flexibilities of experimental investigations. Besides, it used to be difficult to provide the high-resolution data for the researcher to understand the particle dynamics in human lung airways quantitatively and to evaluate the connections among realistic exposure levels, lung uptakes, and health effects. Additionally, the complexity of pre-existing lung diseases and breathing patterns make the personalized exposure health risk assessment even more challenging. Thus, there are knowledge and data gaps of accurate information on how the PM transmits and deposits in the human respiratory system, which is critically needed for more precise health risk studies.

To overcome the drawbacks of those conventional investigating methods, the high-fidelity Computational Fluid-Particle Dynamics (CFPD) models are promising and capable of providing informative high-resolution deposition data based on the natural laws of physics in a noninvasive manner (Dong, Ma, et al., 2018; Feng, Marchal, Sperry, & Yi, 2020; Frederick et al., 2002; Inthavong, Mouritz, Dong, & Tu, 2013; Kleinstreuer & Feng, 2013; Kuga, Ito, Chen, Wang, & Kumagai, 2020; Kuga et al., 2018; Longest & Oldham, 2006; Shimazaki, Okubo, Yamamoto, & Yoshida, 2009; Tian, Ahmadi, Wang, & Hopke, 2012; Tian, Inthavong, Lidén, Shang, & Tu, 2016; Xi & Longest, 2007; Zhao, Feng, Bezerra, Wang, & Sperry, 2019). Indeed, the development of fluid dynamics, computational science, and medical imaging disciplines has spawned a new flourishing interdisciplinary research field in modeling the transport, deposition, and translocation of airborne PM from the indoor environment to human respiratory systems. Complementing bench, *in vivo* and clinical methods, CFPD models are developed based on first principles, which have the unique potential to unveil the underlying physics and chemistry of airflow and PM in the far-field and the respiratory systems with the "x-ray" visions of how individual PM transport and deposit.

Computational fluid-particle dynamics (CFPD) was developed based on the conservation laws of mass, momentum, and energy of both continuous and discrete phases (Kleinstreuer, 2018). CFPD models have been widely used in aircraft, automobile, and machinery design for many decades, complementing wind-tunnel or other experiments. CFPD models play a critical role in exploring alternate study designs and provide high-resolution data in the noninvasive, cost-effective, and time-saving manner.

In the last several decades, CFPD models have been extensively employed to investigate biofluid mechanics and dynamics problems (Bui, Moon, Chae, Park, & Lee, 2020; Inthavong, 2020; Schroeter, Asgharian, & Kimbell, 2019; Tian & Ahmadi, 2020; Tu, Inthavong, & Ahmadi, 2012). Indeed, fluid dynamics, dissolved species transport, and particle dynamics play significant roles in most of the processes in human respiratory systems. The CFPD methodologies can fill the knowledge gap due to the deficiency of traditional *in vitro* and *in vivo* methods, as well as make breakthroughs to pave the way to establish a reliable and efficient numerical investigation framework for occupational exposure risk assessment on a subject-specific level. The employment of CFPD models will be also beneficial in:

(1) Getting insightful views and deep understandings by visualizing the fundamental aerosol dynamics using different variables, and identifying key parameters that can influence the exposure risks.
(2) Accelerating the research cycle significantly by spotting the key parameters and ranges for more effective *in vitro* and *in vivo* experimental designs.
(3) Boosting the innovation possibilities in a broader domain by using time-saving and cost-effective numerical efforts.

Integrating the Physiologically based Pharmacokinetic/Toxicokinetics (PBPK/TK) models (Corley et al., 2015; Corley et al., 2012; Frederick et al., 2002; A. ; Haghnegahdar, Feng, Chen, & Lin, 2018), the multiscale CFPD-PBPK/TK models are able to predict further the health endpoints of the inhaled PM and vapors associated with the delivered lung dose, i.e., the translocation from the respiratory system to systemic regions. The lung deposition data and translocation data are direct evidence to evaluate potential health risks as a function of different parameters such as ambient ventilation conditions, relative humidity, breathing conditions, etc (Feng, Marchal, Sperry, & Yi, 2020). It can contribute significantly to solving the problem of both dosimetry and the health effects of inhaled toxic particulate matter and optimal therapeutic particle delivery to predetermined lung sites. Therefore, the CFPD-PBPK/TK models are beneficial to quantify the full process of generation, dispersion, and inhalation of airborne PM to ensure a comprehensive characterization of the relationship of potential health risks to individuals with different ventilation and breathing conditions.

This paper serves as both a tutorial and a review on how to employ CFPD-PBPK/TK models to predict the transport, deposition, and translocation of inhaled aerosols from their generation sources to human respiratory systems and the connected systemic regions (i.e., health endpoints) in the whole body. Specifically, key definitions and governing equations are introduced and discussed in Section 2, focusing on the most widely used CFPD and PBPK/TK modeling framework for computational lung aerosol dynamics simulations. For the tutorial purpose, Section 3 provides a step-by-step guide on how to perform computational lung aerosol dynamics simulations using CFPD and PBPK/TK methods, with details on (a) the importance of corrected reconstruction of surface smoothness of the pulmonary airways from computed tomography/magnetic resonance imaging (CT/MRI) scan data; (b) the significance of choosing the appropriate turbulence model to predict the laminar-to-turbulence pulmonary airflow regimes; (c) the standard validation and verification procedures of submodels in the CFPD-PBPK/TK modeling framework; and (d) the available different multiphase flow models and their distinct advantages on modeling different types of aerosols. As the challenges of the current modeling procedure, the

key assumptions and simplifications used in most of the popular computational lung aerosol dynamics models are listed in Section 4, with several on-going research efforts on developing the next-generation computational lung aerosol dynamics models by encompassing more physiologically realistic mechanisms.

2. Theory

2.1. Key concepts for CFPD-PBPK/TK model development

Interdisciplinary fundamental knowledge is needed to perform scientific and rigorous CFPD-PBPK/TK simulations for lung aerosol dynamics. The map of the fundamental knowledge and concepts needed to develop and perform the CFPD-PBPK/TK model is shown in Fig. 1. Many factors can play a role in the dynamic behaviors of PM and vapors/gases simultaneously, i.e.,

(1) The respiratory tract geometry. Geometric variations have a substantial impact on the flow field (Feng et al., 2018). Both subject variability and health conditions can significantly alter the anatomical features of the human respiratory systems. For example, Airway opening diameters can be quite different between healthy and diseased lung such as chronic obstructive pulmonary disease (COPD), which is characterized by airway obstructions and (Hajian et al., 2018; McLellan et al., 2020; van Geffen et al., 2018). Different airway geometries will generate unique airflow patterns and hence cause different localized particle deposition patterns, due to impaction as well as secondary flows, diffusion and/or gravity. Also, different geometries may induce a great change of local Reynolds numbers for a given inlet velocity, leading to differences in locally transitional flow characteristics.
(2) The breathing patterns, e.g., inhalation/exhalation waveforms, maximum and mean flow rates, and frequency.
(3) PM properties, e.g., particle size, shape, density, hygroscopicity, and surface properties.

To establish the governing equation system correctly, the following aspects need to be understood first to identify the air-vapor/gas-PM multiphase flow dynamics:

(1) Airflow Dynamics (Fluid Rheology):
- Is the flow steady-state or transient?
- Is the flow laminar, or turbulence, or containing laminar-to-turbulence transition?
(2) Fluid-Particle Dynamics of Secondary Phases:

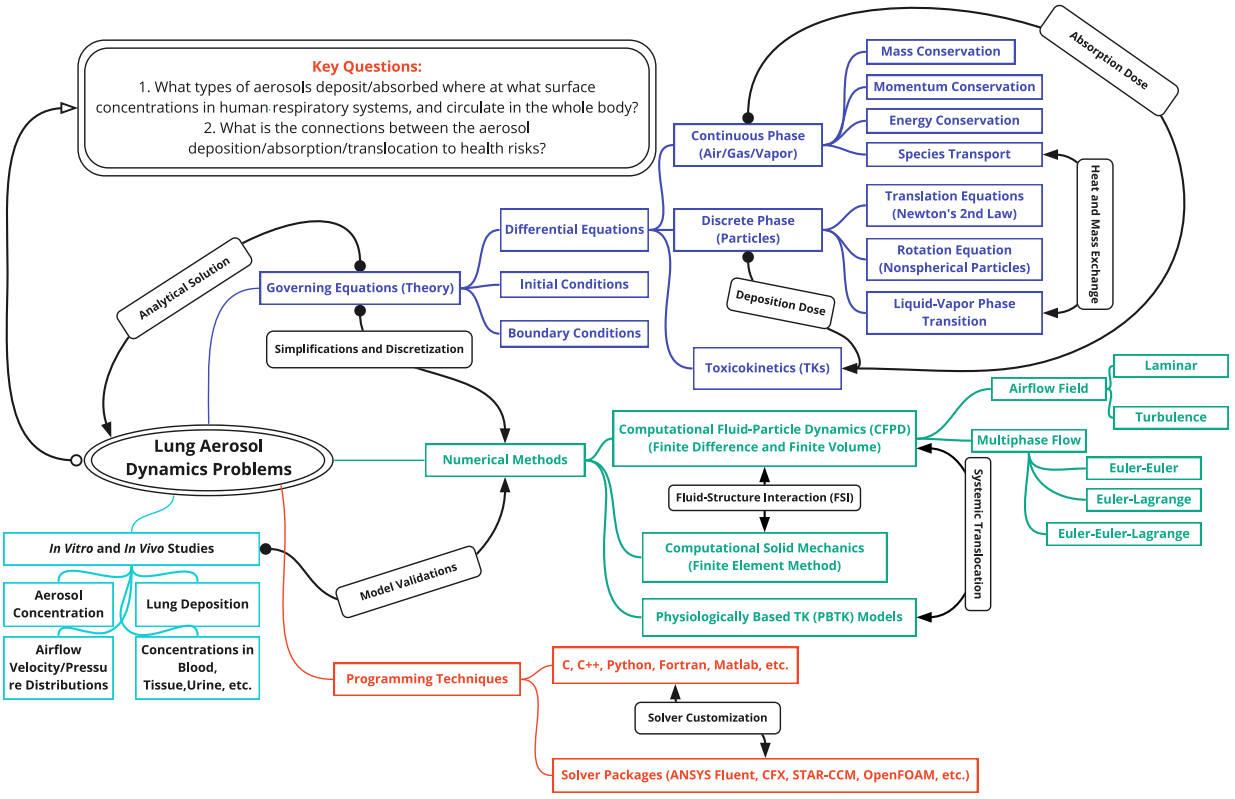

Fig. 1. The fundamental knowledge map for CFPD-PBPK/TK model development and execution.

- Is the PM suspension dilute (non-interacting one-way coupled Euler-Lagrange method) or dense (interacting two-way coupled Euler-Lagrange method or using other numerical methods)?
- Is the PM hygroscopic (diameters change with time)?
- Is there any continuous vapor/gas phase that needs to be investigated (Euler-Euler method)?

(3) Heat Transfer:
- What heat transfer mechanisms need to be considered, i.e., conduction, convection, and/or radiation?

(4) Fluid-Structure Interactions (FSIs):
- Can the airway contraction/expansion motion neglected or must be considered?

The following subsections focus on presenting the governing equations for the predictions of pulmonary airflow and aerosol dynamics as well as the subsequent toxicokinetics, emphasizing the importance of the closure of the equation system.

2.2. Governing equations

2.2.1. CFPD model

2.2.1.1. Primary phase: airflow. The airflow dynamics in the ambient environment and the respiratory tract are usually unsteady, driven by ventilation and the cyclic breathing processes. To accurately predict airflow fields containing both laminar and turbulence regimes, the incompressible Navier-Stokes (N-S) equation is employed to characterize airflow in the human respiratory tract, accompanied by continuity equation, energy equation, and constitutive equations, i.e.,

Continuity Equation

$$\frac{\partial u_j}{\partial x_j} = 0 \tag{1}$$

in which u_j represents the air velocity, and ρ is the air density.

Navier-Stokes (N-S) Equation

$$\rho\left(\frac{\partial u_i}{\partial t} + \frac{\partial\left(u_i u_j\right)}{\partial x_j}\right) = -\frac{\partial p}{\partial x_i} + \frac{\partial \tau_{ij}}{\partial x_j} + \rho g_i \tag{2}$$

where p is the pressure, $g_i$is the gravitational acceleration. The viscous stress tensor τ_{ij} in Eq. (2) can be given by:

$$\tau_{ij} = \mu\left(\frac{\partial u_i}{\partial x_j} + \frac{\partial u_j}{\partial x_i}\right) \tag{3}$$

where μ is the air viscosity.

Energy Equation

$$\rho\frac{\partial\left(c_p T\right)}{\partial t} + \rho\frac{\partial\left(c_p u_j T\right)}{\partial x_j} = \frac{\partial}{\partial x_j}\left[k\frac{\partial T}{\partial x_j}\right] + \Phi + S_T \tag{4}$$

where T is the temperature, k is thermal conductivity and c_p is specific heat capacity. Furthermore, S_T is the thermal sink or source term due to the heat exchange of phase change induced by condensation or evaporation. Φ is the dissipation function which can be given as:

$$\Phi = \tau_{ij}\frac{\partial u_i}{\partial x_j} \tag{5}$$

2.2.1.2. Secondary Lagrangian phase: discrete particulate matter (PM). To track PM using the Euler-Lagrange method (Kleinstreuer, 2003; Kleinstreuer & Zhang, 2010), the kinematics of a particle in the airflow needs to be correctly predicted, which depends on the accurate description of external forces imposed on the particle by the suspending medium or carrier fluid. The Euler-Lagrange method, which is also called the discrete phase model (DPM), provides a direct description of the particulate flow by tracking the motion of individual particles. The continuous phase, i.e., airflow, is governed by conservation laws which can be solved as the Eulerian phase (see Eqs. (1)–(5)). For spherical particles, their motions are governed by Newton's 2nd law, which employs empirical correlations for hydraulic forces acting on the particles (Kleinstreuer, 2003; Kleinstreuer & Feng, 2013; Kleinstreuer & Zhang, 2010). For dilute particle suspensions, the one-way coupled Euler-Lagrange method is eligible to be applied, indicating the particle motion is influenced by the flow field, while the flow field is not disturbed by the particles. Specifically, for an individual particle, the trajectory can be obtained by solving the particle motion equation, i.e.,

$$\frac{d}{dt}\left(m_p \overrightarrow{u^p}\right) = \sum \vec{F}_{body} + \sum \vec{F}_{surface} + \sum \vec{F}_{interaction} \tag{6}$$

In Eq. (6), forces acting on the particles are categorized into three terms: (1) $\sum \vec{F}_{body}$are body forces which are proportional to the

particle mass, (2) $\sum \vec{F}_{surface}$ are surface forces of which the magnitudes are proportional to the particle surface area and related to the surrounding fluid stress, and (3) $\sum \vec{F}_{interaction}$ are particle-particle and particle-wall interactions. Forces may be considered in Eq. (6) are listed as follows:

$$\sum \vec{F}_{body} = \vec{F}_G + \vec{F}_{buoyancy} + \vec{F}_{VM} + \vec{F}_{BM} \tag{7}$$

$$\sum \vec{F}_{surface} = \vec{F}_D + \vec{F}_{pressure} + \vec{F}_{Saffman} \tag{8}$$

$$\sum \vec{F}_{interaction} = \vec{F}_{particle-particle} + \vec{F}_{particle-wall} \tag{9}$$

where $\vec{F}_G$ is the gravity, $\vec{F}_{buoyancy}$ is the buoyancy force (Johnson, 2016), $\vec{F}_{VM}$ is the virtual mass force (Johnson, 2016), $\vec{F}_{BM}$ is the Brownian motion induced force (Li & Ahmadi, 1993) $\vec{F}_D$ is the Stokes drag force (Kleinstreuer, 2003; Kleinstreuer & Feng, 2013; Kleinstreuer & Zhang, 2010), $\vec{F}_{pressure}$ is the pressure gradient force (Shimazaki et al., 2009), $\vec{F}_{Saffman}$ is the Saffman lift force (Saffman, 1965), $\vec{F}_{particle-particle}$ is the summation of adhesive and repulsive forces between particles (Norouzi, Zarghami, Sotudeh-Gharebagh, & Mostoufi, 2016), and $\vec{F}_{particle-wall}$ is the summation of adhesive and repulsive forces between particles and wall boundaries. It should be emphasized that $\vec{F}_{BM}$ is included in Eq. (7), because the Brownian motion induced force is numerically treated as an additional body force in the CFPD-PBPK/TK model (Li & Ahmadi, 1993; Michaelides, 2003).

Not all forces in Eqs. (7)–(9) are necessary to be considered, since some of them may be negligible compared with other forces in magnitude. The relative order of magnitude analysis (ROMA) (Kleinstreuer, 2003; Kleinstreuer & Zhang, 2010) should be done to determine the forces that need to be considered in Eq. (6), to guarantee the accuracy and computational efficiency of employed models. Usually, the relative importance of forces are determined based on the comparison with $\vec{F}_D$. Examples of ROMA can be found in (Kleinstreuer, 2003; Kleinstreuer & Feng, 2013; Kleinstreuer & Zhang, 2010).

It is worth mentioning that most existing CFPD models assume that particles are spherical and treat them as mass points (Feng, Xu, & Haghnegahdar, 2016; Tu et al., 2012; Xi, Kim, & Si, 2016). Equation (6) can be complex as it includes a wide range of length scales and time scales as well as issues concerning turbulence, convection, settling, two-way coupling, collisions, aggregation, etc. For instance, most of the airborne particles are non-spherical, and some of them are highly anisotropic in shape, such as fiber-like particles, of which the rotational motions should be accurately predicted (Feng & Kleinstreuer, 2013a; Kleinstreuer & Feng, 2013; Tian & Ahmadi, 2020)). Furthermore, particles or droplets may also change in size during the transport by condensation and evaporation effect (Guo et al., 2020), which need to be accurately captured since the PM size change can significantly influence their trajectories and deposition locations (Feng, Kleinstreuer, Castro, & Rostami, 2016; Feng, Kleinstreuer, & Rostami, 2015; Feng et al., 2020; Haghnegahdar, Zhao, & Feng, 2019). Therefore, supplementary equations must be included. Details can be found in existing review papers (Bui et al., 2020; Xi et al., 2016; Feng et al., 2016; Inthavong, 2020; Schroeter et al., 2019; Tian & Ahmadi, 2020; Tu et al., 2012).

2.2.1.3. Secondary Eulerian phase: vapor/gas. Toxic gases and vapors can be harmful to the pulmonary tract *via* inhalation. Their transport phenomena can be predicted by solving species transport equations with or without turbulence dispersion (Zhao et al., 2019), i.e.,

$$\frac{\partial(\rho_{a-g}Y_s)}{\partial t} + \frac{\partial(\rho_{a-g}u_jY_s)}{\partial x_j} = \frac{\partial}{\partial x_j}\left[\left(\rho_{a-g}\widetilde{D}_{a-g,s} + \frac{\mu_t}{\sigma_Y}\right)\frac{\partial Y_s}{\partial x_j}\right] + S_{v-d}^{(Y_S)} \tag{10}$$

where Y_s is the mass fraction of the s-th gas/vapor species, σ_Y is the turbulent Schmidt number (Feng, Kleinstreuer, Castro, & Rostami, 2016), μ_t is the turbulence viscosity, ρ_{a-g} is the mixture density, and $\widetilde{D}_{a-g,s}$ is the molecular diffusivity of the s-th gas species in the air, which can be either estimated using the Stokes-Einstein equation (Einstein, 1908) or directly obtained from experimental measurements and discrete particle trajectory simulations. $S_{v-d}^{(Y_S)}$ is the source term to characterize phase changes between the vapor and liquid, because of the evaporation and condensation. $S_{v-d}^{(Y_S)}$ can be given by:

$$S_{v-d,s}^{(Y)} = \frac{\sum_{i=1}^{N_{d,cell}}\left(\overline{j}_s A_d\right)_i}{V_{cell}} \tag{11}$$

where $\overline{j}_s$ is the average evaporation/condensation mass flux normal to the droplet surface of the s-th component (i.e., $\overline{j}_s > 0$ for evaporation and $\overline{j}_s < 0$ for condensation). A_d is the droplet surface area. For solid particles simulations with constant particle diameters, $S_{v-d}^{(Y_S)} = 0$.

2.2.2. PBPK/TK model

Lung deposition sites are not health endpoints. Toxicologists, pharmacists, and clinicians are more interested in the after-deposition dynamics, i.e., the time courses of therapeutic or toxic species in plasma and organs through the human body. To extend the lung

aerosol dynamics simulation to PK/TK health endpoints, PBPK/TK models can be integrated with the CFPD model (see Fig. 2 for the modeling framework) to predict the systemic translocation after the deposition and absorption in the respiratory system (Corley et al., 2015; Corley et al., 2012; Frederick et al., 2002; Haghnegahdar et al., 2018). Specifically, the PBPK/TK models can:

(1) Predict plasma, tissue, and urine levels of certain species,
(2) Estimate possible accumulations of drugs/toxicants as well as their metabolites, and
(3) Correlate concentrations directly with the toxicologic activities.

As shown in Fig. 2, the prediction of the transport from the airways to the systemic region is performed by calculating the absorption and deposition in the respiratory system using the CFPD model as the input to the PBTK model. Using a perfusion-limited model as an example (see Fig. 2), the PBTK modelusually consists of multiple coupled organs. Each organ is modeled as a well-mixed compartment. Concentrations $C_T$in compartments other than the venous blood pool are governed by a generalized time-dependent ordinary differential equation (ODE), i.e.,

$$V_T \frac{d}{dt} C_T = Q_T . \left(C_{ART,\ in} - \frac{C_T}{K_T} \right) - IC_M \frac{C_T}{K_T} \tag{12}$$

where V_T, Q_T, and K_T are the compartment volume, blood flow rate, and tissue-blood partition coefficient of compartment T representing a certain organ or tissue group. $C_{ART,\ in}$ is the concentration in the arterial blood pool, which is equal to the total deposition/absorption concentration in the pulmonary system which can be obtained from CFPD simulation results (see Fig. 2). In Eq. (12), subscript T can represent muscle (MUS), vessel-rich tissue (VRT), fat group (FAT), kidney (KID), liver (LIV), and gastrointestinal tract (GIT). Physiologically realistic data of V_T and Q_T are listed in Table 1 (Katz, Murdock, Palgen, Pype, & Caillibotte, 2015) for an adult male subject. Additionally, $C_{T,\ in}$ is the input concentration to the organs, which is equal to the concentration in the arterial pool. IC_M represents the intrinsic hepatic clearance or renal clearance. The elimination term is equal to zero for non-eliminating organs. For venous blood pool compartment, Eq. (12) can be rewritten as:

$$V_{VEN} \frac{d}{dt} C_{VEN} = Q_{VEN} . C_{VEN,\ in} - Q_{LUNG} C_{VEN} \tag{13}$$

It is worth mentioning that the input concentration $C_{VEN,\text{in}}$ for the venous pool is the averaged amalgamation of interconnected organs to the venous pool, which is given by:

$$C_{VEN,\ in} = \frac{1}{Q_{VEN}} \sum_T \frac{Q_T C_T}{K_T} \tag{14}$$

where Q_V the cardiac output, representing the total volumetric flow rate of blood circulation (see Table 1). Parameters, including the volume and flow rate of organs, cardiac output, alveolar ventilation, body weight, and blood/tissue-gas partition coefficients, need to be obtained from open literature or calibrated via multi-parameter optimizations based on available clinical data or animal studies (Haghnegahdar et al., 2018; Haghnegahdar, Zhao, & Feng, 2019).

In addition to PBPK/TK models, CFPD models can also be connected with Host Cell Dynamics (HCD) models, and track virus-laden droplet deposition, transport, and the triggered immune system responses (Haghnegahdar, Zhao, & Feng, 2019). Specifically, the HCD models are able to interconnect cell count changes among viruses, interferons, natural killer (NK) cells, T cells, B cells, etc.

2.2.3. *Interconnections between CFPD and PBPK/TK models*

The biokinetics, i.e., the after-deposition dynamics, of inhaled PM and gas/vapor depends on various factors, such as the vapor/gas solubilities in the mucus layer, saturation behavior, thickness of the tissue, and the site of deposition. Specifically, the absorption of those aerosol species is driven by concentration differences in between the tissue and air. Once absorbed in the tissue, the species are dissolved in the mucus layer. The dissolved species then diffuses through the tissue layers before it is finally cleared by the blood circulatory system. The diffusion of particles through the walls of the conducting airways can be modeled with an appropriate species-mass transfer equation. The diffusion of deposited particles into the systemic region depends on the tissue structure of the airways. The

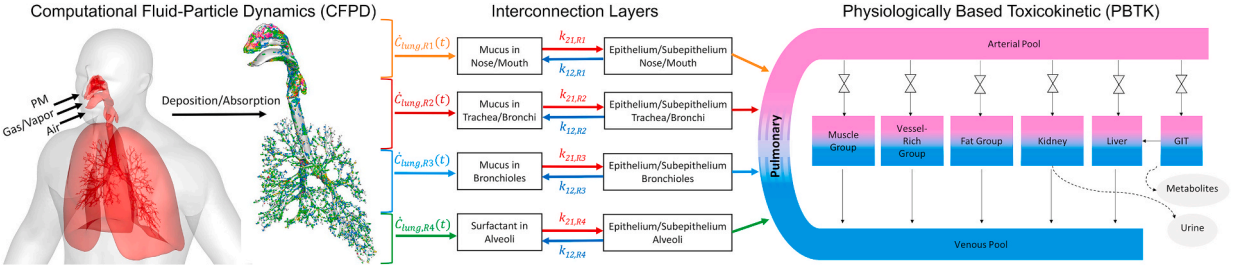

Fig. 2. Schematic of the proposed multiscale CFPD-PBPK/TK modeling framework.

Table 1
Human physiological parameters for Eqs. (12) and (13).

Compartment Name	Abbreviation (T)	Volume V_T [L]	Blood Flow Q_T [L/min]
Arterial Pool	ART	1.46	6.0
Venous Pool	VEN	3.82	6.0
Lung Blood	LUNG	0.17	6.0
Fat (Richly Perfused)	FATR	6.30	0.24
Fat (Poorly Perfused)	FATP	4.20	0.06
Liver	LIV	4.37	1.56
Tissue (Richly Perfused)	VRT	16.80	1.98
Tissue (Poorly Perfused)	VPT	30.80	0.06
Muscle	MUS	1.23	1.44
Brain	BR	1.46	0.558
Body Weight [kg]	70 (Adult Male Human)		
Cardiac Output Q_{VEN} [L/min]	6.0		

conducting airways consist of the nasal, oral, pharyngeal, and tracheobronchial airways, where the walls are covered with a protective mucus layer. The mucus layer is situated over the ciliated epithelium tissue. The mucus thickness can vary from 8.3 μm in the trachea to 1.8 μm in the lower bronchioles (Asgharian, Hofmann, & Miller, 2001; Hofmann & Sturm, 2004). As the inputs to the PBPK/TK model, the deposition and absorption flow rates $\dot{C}_{lung,\,Rk}(t)$ calculated using the CFPD model should be obtained, with the multilayer-tissue interconnection model (Corley et al., 2012, 2015) (see Fig. 2). The simulation process for humans will include convection-diffusion of PM/gas/vapor through the air medium, absorption at the air-tissue interface, diffusion through the mucus/tissue, diffusion into the blood circulatory system, and transport to organs. The schematic representation of the interconnection model between CFPD and PBPK/TK with transfer coefficients is shown in Fig. 2. The number of "other organs" can be found in Fig. 2. The compartments are connected based on the transfer routes. As the airway tissue properties are region-specific, the model is divided into nasal/oral region ($Rk = R1$), trachea-to-bronchi region ($Rk = R2$), bronchiolar region ($Rk = R3$), and alveolar region ($Rk = R4$). The amount of aerosol

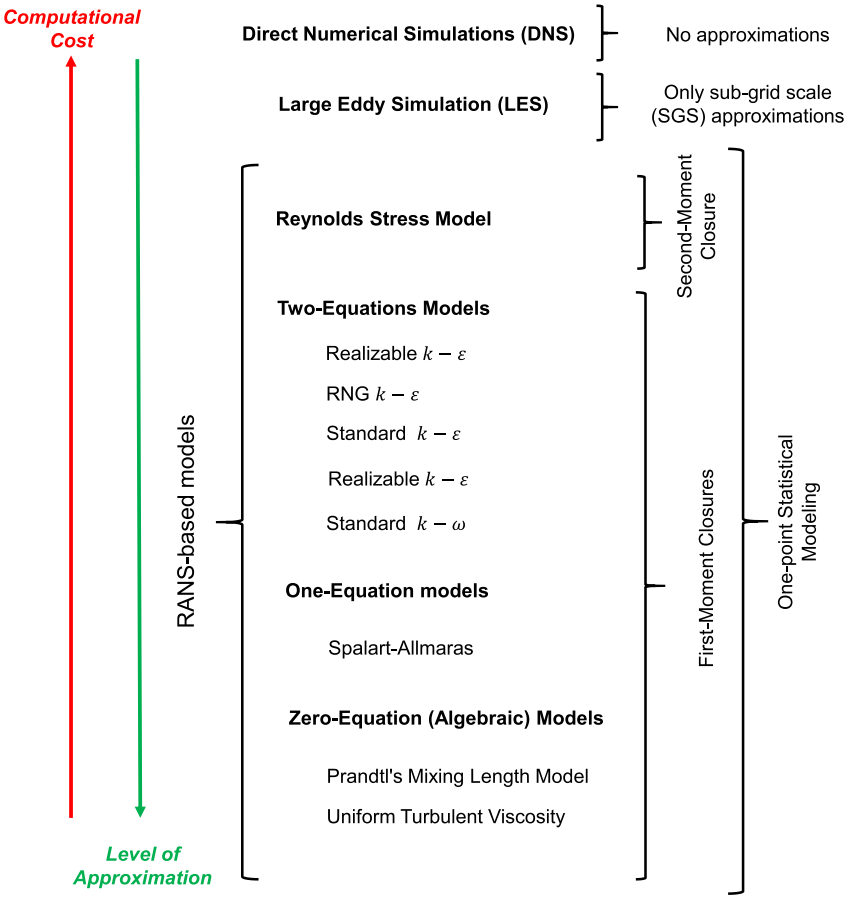

Fig. 3. Overview of the computational efficiency and resolution for different turbulence models.

Table 2
SGS models employed in pulmonary aerosol dynamics simulations.

SGS Model	Equations	Pros	Cons	References
Smagorinsky	$\upsilon_T = L_s^2\left\|\overline{S}\right\|$ where $L_s = \min(\kappa d_w, C_s\Delta)$, $\left\|\overline{S}\right\| = \sqrt{2\overline{S}_{ij}\overline{S}_{ij}}$, $\overline{S}_{ij} = \frac{1}{2}\left(\frac{\partial\overline{u}_i}{\partial x_j} + \frac{\partial\overline{u}_j}{\partial x_i}\right)$, $\kappa = 0.41$ is the von Kármán constant,and Δ is computed according to the volume of the computational cell using $\Delta = V^{1/3}$ (Smagorinsky, 1963).	1. Simplest SGS model with only one adjustable parameter, i.e., C_s, for modeling eddy-viscosity 2. Good computational stability 3. Good results for homogeneous isotropic turbulence in the inertial subrange	1. The adjustable parameter is not a universal constant 2. Produces nonzero turbulent viscosity 3. Excessive damping of large-scale fluctuations in the presence of mean shear and in transitional flows as near solid boundary	(Xinguang Cui, Wu, & Gutheil, 2018; Farghadan et al., 2020; Jayaraju, Brouns, Lacor, Belkassem, & Verbanck, 2008; Jin et al., 2007; Kannan et al., 2017; Nagels & Cater, 2009)
Dynamic Smagorinsky	$\tau_{ij} = -2C\overline{\rho}\Delta^2\left\|\overline{S}\right\|\left(\overline{S}_{ij} - \frac{1}{3}\overline{S}_{kk}\delta_{ij}\right)$ with $C = \frac{(L_{ij} - L_{kk}\delta_{ij}/3)M_{ij}}{M_{ij}M_{ij}}$ $C_s = \sqrt{C}$. Details regarding the above expressions can be found in literatures (Germano, Piomelli, Moin, & Cabot, 1991; Kim, 2004; Lilly, 1992).	1. Easy implementation (no need for users to specify the model constant C_s, as it is dynamically computed based on the information provided by the resolved scales of motion) 2. Varying value of C_s in time and space over a fairly wide range	1. Higher computational cost than Smagorinsky model, since two filters are applied to the equation of motion 2. Under-prediction of turbulence level for wall bounded flows (high dissipation rate) 3. Algorithm needs to be locally averaged to avoid numerical instability	(Hariprasad et al., 2020; Islam, Saha, Sauret, Gemci, & Gu, 2017; Koullapis, Nicolaou, & Kassinos, 2018; Koullapis, Nicolaou, & Kassinos, 2018)
WALE	$\upsilon_T = L_s^2\frac{(S_{ij}^d S_{ij}^d)^{3/2}}{(\overline{S}_{ij}\overline{S}_{ij})^{5/2} + (S_{ij}^d S_{ij}^d)^{5/4}}$ where $L_s = \min(\kappa d_w, C_w\Delta)$ and $S_{ij}^d = \frac{\partial\overline{u}_i}{\partial x_j}$ (Nicoud & Ducros, 1999).	1. Designed to return the correct wall asymptotic behavior for wall bounded flows 2. Return a zero turbulent viscosity for laminar shear flows, which allows the correct treatment of laminar zones in the domain 3. Better prediction at near wall region than dynamic Smagorinsky model	1. Less accuracy in terms of estimating the peaks of the velocity fluctuations and the *r.m.s.* of the wall-pressure distribution than dynamic Smagorinsky model (Ben-Nasr, Hadjadj, Chaudhuri, & Shadloo, 2017)	(Alzahrany, Banerjee, & Salzman, 2014; Alzahrany, 2014; Farghadan et al., 2020; Jayaraju, Brouns, Lacor, Belkassem, & Verbanck, 2008; Koullapis et al., 2018)
Vreman	$\upsilon_T = C\sqrt{\frac{B_\beta}{S_{ij}^d S_{ij}^d}}$ with $S_{ij}^d = \frac{\partial\overline{u}_i}{\partial x_j}$, $\beta_{ij} = \Delta_m^2\alpha_{mi}\alpha_{mj}$, $B_\beta = \beta_{11}\beta_{22} - \beta_{12}^2 + \beta_{11}\beta_{33} - \beta_{13}^2 + \beta_{22}\beta_{33} - \beta_{23}^2$. Constant C is related to the Smagorinsky constant C_s by $C \approx 2.5C_s^2$ (Vreman, 2004).	1. Comparable performance to the dynamic Smagorinsky model 2. Anisotropic nature requiring no wall-damping functions 3. Can handle not only turbulent flow but also transitional flow 4. Yield zero SGS dissipation for various laminar shear flows	1. Currently not available in commercial software, e.g., Fluent; need to develop own source code (time consuming)	(Choi, Tawhai, Hoffman, & Lin, 2009; Lambert, O'Shaughnessy, Tawhai, Hoffman, & Lin, 2011; Yin et al., 2010)

species in each compartment can be calculated by assuming mass balances among compartments. The mass balance equation for compartment i can be written as:

$$\frac{dC_{i,Rk}}{dt} = k_{ji,Rk}C_{j,Rk} - k_{ij,Rk}C_{i,Rk} + \dot{C}_{lung,\ Rk}(t) \tag{15}$$

where k_{ij} and k_{ji} are the transfer rate constants from compartment i to compartment j, and from compartment j to compartment i, and $\dot{C}_{lung,\ Rk}(t)$is the absorption and deposition rate through the lung, which can be obtained from CFPD simulation results. Specifically, i = 1 or j = 1 indicates the mucus layers or surfactant layer in R4, while i = 2 or j = 2 represent the epithelium/subepithelium layers (see Fig. 2). The transfer rates $k_{ij,Rk}$ can be estimated by $k_{ij,Rk} = D_{ab}/h^2$, where D_{ab} is the diffusivity of the vapor through each medium, and h denotes the compartmental thickness. $k_{ij,Rk}$ can be calibrated with concentration profiles obtained in *in vitro* and *in vivo* studies. Specifically, drug/toxicant and their metabolite concentrations in blood, plasma, and serum can be obtained via blood sampling. Concentrations in tissues can be obtained via tissue biopsy. In addition, concentrations in urine and saliva can also be used for model calibration. In addition, the subscript *Rk* (k=1,2,3, and 4) indicate the four regions of the human respiratory systems (see Fig. 2).

2.2.4. Governing equation modifications for different turbulence models

Covering a broad spectrum of flow regimes, the airflow field in human respiratory systems contains transitions between laminar and turbulence (Banko, Coletti, Schiavazzi, Elkins, & Eaton, 2015; Bernate, Geisler, Padhy, Shaqfeh, & Iaccarino, 2017). Specifically, airflows transform from laminar to turbulence when passing the glottis and entering the trachea (Zhao et al., 2020). The airflow regime gradually shifts to laminar again from the trachea to small airways (Kolanjiyil & Kleinstreuer, 2017; Koullapis, Nicolaou, & Kassinos, 2018; Longest, Tian, Delvadia, & Hindle, 2012). Flows will even change to creeping flows in the alveoli (Kolanjiyil, Kleinstreuer, & Sadikot, 2017; Koullapis, Hofemeier, Sznitman, & Kassinosa, 2018b; Longest, Tian, Delvadia, & Hindle, 2012). It is crucial to select appropriate turbulence models to capture the transition onset accurately with affordable computational cost, since the airflow field will significantly influence the PM and vapor/gas transport dynamics especially through the pulmonary routes. Three different methods can be applied to solve the turbulent flow: direct numerical simulations (DNS) (Wang & Elghobashi, 2014), Reynolds-averaged Navier-Stokes (RANS) (Y Feng & C Kleinstreuer, 2013; Feng et al., 2018; Zheng, 2011), and Large Eddy Simulations (LES) (Cui and Gutheil, 2018). Although DNS solves the full unsteady N-S equations and can resolve the whole spectrum of turbulent scales (Wang & Elghobashi, 2014), the computational cost for using it in the complex flow domains such as the respiratory system is too high and not practical for the lung aerosol dynamics study (Thäter, 2016). Therefore, two RANS and LES models are discussed in this section. The comparisons of other turbulence models are shown in Fig. 3.

2.2.4.1. Reynolds averaged Navier-Stokes (RANS) models. To capture the airflow structures in the laminar-to-turbulent flow regimes in human upper airways under common inhalation flow rates, the low-Reynolds-number (LRN) k-ω model and shear stress transport (SST) transition model are selected and adapted (Y Feng & C Kleinstreuer, 2013; Feng et al., 2018; Zheng, 2011), based on their overall performance in predicting the onset of "laminar-to-turbulent" transition, their computational efficiency and reasonable accuracy as compared with large eddy simulations (LES). Using the Reynolds decomposition (Wilcox, 1998), the momentum equation (Eq. (2)) can be rewritten as the Reynolds averaged Navier-Stokes (RANS) equation, i.e.,

$$\frac{\partial \overline{u_i}}{\partial t} + \overline{u_j}\frac{\partial \overline{u_i}}{\partial x_j} = -\frac{1}{\rho}\frac{\partial \overline{p}}{\partial x_i} + \upsilon\frac{\partial^2 \overline{u_i}}{\partial x_i \partial x_j} + \frac{1}{\rho}\frac{\partial\left(-\rho\overline{u_i' u_j'}\right)}{\partial x_j} + g_i \tag{16}$$

where $\overline{u_i}$ is the time-average velocity component and u_i' is the fluctuation component of the velocity, and $-\rho\overline{u_i' u_j'}$ is the Reynolds stress tensor. RANS models all focus on how to introduce supplementary equations to solve the fluctuation components as the new unknown in $-\rho\overline{u_i' u_j'}$. Using $k-\varepsilon$ based two-equation RANS models as an example, $-\rho\overline{u_i' u_j'}$. can be rewritten based on Boussinesq hypothesis (Wilcox, 1998) as:

$$-\rho\overline{u_i' u_j'} = \mu_T\left(\frac{\partial \overline{u_i}}{\partial x_j} + \frac{\partial \overline{u_j}}{\partial x_i}\right) - \frac{2}{3}\left(\rho k + \mu_T\frac{\partial \overline{u_k}}{\partial x_k}\right)\delta_{ij} \tag{17}$$

where k is the turbulent kinetic energy, and μ_T is the eddy viscosity which can be expressed by:

$$\mu_T = C_\mu\frac{k^2}{\varepsilon} \tag{18}$$

where C_μ is coefficient that can be calibrated with fluid dynamics experiments, and ε is the rate of dissipation of turbulent kinetic energy k. Thus, using Eqs. (16) and (17), the Reynolds stress tensor can be solved by introducing two additional transport equations for k and ε (Wilcox, 1998). For other types of RANS models, the key is to introduce a model to define μ_T and solve the Reynolds stress tensor by introducing additional transport equations for additional variables.

For these Reynolds averaged Navier-Stokes (RANS) models, only averaged values of velocity, pressure, and other turbulence variables are calculated. When employing RANS models, the following aspects need to be carefully examined:

(1) The prediction of the fluctuation velocities of the laminar-turbulence-laminar flow transitions in upper airways is not available using RANS models. The instantaneous fluctuation components can be recovered, which is approximated by the eddy-interaction model (EIM) (Graham & James, 1996; Graham, 1998). Due to the anisotropic characteristics of the near-wall fluctuation velocities, near-wall corrections when using RANS model must be considered (Y Feng & C Kleinstreuer, 2013; Feng et al., 2018; Zheng, 2011). It has a strong effect on heat transfer predictions in reattachment and stagnation regions.
(2) The near-wall formulation of a turbulence model has a substantial effect on its accuracy and its robustness. Therefore, y + needs to be correctly set up (see Section 3.2.1.2 for detailed suggestions).

Recently, a versatile RANS model, i.e., the generalized k-ω (GEKO) model (Menter, Matyushenko, & Lechner, 2018), has been widely used which consolidates two-equation models (Wilcox, 1998). The GEKO model is y + insensitive and with better convergence performances. Therefore, with appropriate calibrations, the GEKO model can be considered to be used for pulmonary airflow field simulations.

2.2.4.2. Large eddy simulation (LES). Compared with DNS and RANS, LES solves large scales of turbulence directly and resolves the small scales using subgrid-scale models based on the Boussinesq hypothesis (Cui & Gutheil, 2018; Jin, Fan, Zeng, & Cen, 2007; Kenjereš & Tjin, 2017; Koullapis, Nicolaou, & Kassinos, 2018; Xi et al., 2015b; Xi et al., 2016). LES retains significantly more elements of the underlying turbulence physics with an affordable computation cost, which will be more widely adopted in the next five years with a boost in computational power worldwide. In addition, due to the fact that momentum, mass, energy, and concentrations are transported by large eddies, LES is capable of accurately capture the turbulence in large scale. Meanwhile, small eddies are more isotropic, so subgrid-scale (SGS) models are reasonably accurate to solve the small-scale turbulence. Specifically, a filtering decomposition is introduced for u_i as:

$$u_i = \overline{u_i} + u_i' \tag{19}$$

where c is the velocity component at the resolved scale (large scale), and u_i' is the component at the sub-grid scale (SGS). $\overline{u_i}$ is a local average of the anisotropic velocity fields that can be directly resolved, which can be determined using a filter function G, i.e.,

$$\overline{u_i}(\vec{x}) = \int G(\vec{x} - \vec{\xi}) u_i(\vec{\xi}) d\vec{\xi} \tag{20}$$

G is equal to 0 if $|\vec{x} - \vec{\xi}|$ is less than certain filter width Δ (e.g., the mesh cell characteristic length), which will filter out u_i' in SGS.

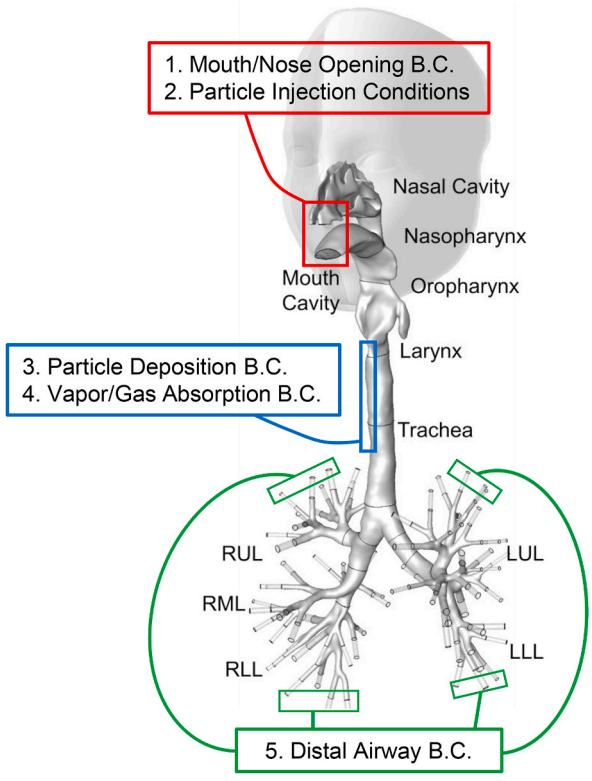

Fig. 4. Essential boundary conditions used for computational lung aerosol dynamics.

The commonly used filter functions can be found in (Mason, 1994). Integrating Eq. (2) using the filter function G, Eq. (2) can be changed into the filtered N-S equation, i.e.,

$$\frac{\partial \overline{u_i}}{\partial t}+\overline{u_j}\frac{\partial \overline{u_i}}{\partial x_j}=-\frac{1}{\rho}\frac{\partial \overline{p}}{\partial x_i}+\upsilon\frac{\partial^2 \overline{u_i}}{\partial x_i \partial x_j}+\frac{1}{\rho}\frac{\partial \tau_{ij}}{\partial x_j}+g_i \tag{21}$$

where τ_{ij} is the sub-grid scale (SGS) stress, which can be given by

$$\tau_{ij}=\overline{u_i u_j}-\overline{u_i}\,\overline{u_j} \tag{22}$$

Using the Boussinesq hypothesis, Eq. (20) can be rewritten to:

$$\frac{\partial \overline{u_i}}{\partial t}+\overline{u_j}\frac{\partial \overline{u_i}}{\partial x_j}=-\frac{1}{\rho}\frac{\partial \overline{p}}{\partial x_i}+\frac{\partial}{\partial x_j}\left((\upsilon+\upsilon_T)\frac{\partial \overline{u_i}}{\partial x_j}\right)+g_i \tag{23}$$

Thus, the key to solve Eq. (23) is to find appropriate SGS models for the eddy viscosity υ_T. Available SGS models that have been employed in lung aerosol dynamics simulations are listed in Table 2.

2.2.5. *Boundary conditions*

Generally, boundary conditions (B.C.s) are "statements" describing how numerial simulations reflect surrounding environments. Accurate CFPD-PBPK/TK simulations also require physiologically realistic boundary conditions (see Fig. 4). Discussion of B.C.s includes two questions: (1) how many B.C.s are needed to find deterministic solutions of the governing equation system, and (2) what B.C.s are they. For the first question, it was predetermined by the numbers of variables and orders of the differential equations. The following discussion is in Question 2, i.e., what appropriate B.C.s should be given.

2.2.5.1. Mouth/nose opening boundary conditions. At the mouth or nose openings, boundary conditions (B.C.s) need to be defined are listed as follows:

(1) Airflow velocity or flow rate *vs.* time to characterize human breathing waveforms, i.e., $u_i(t)|_{mouth/nose}=U_i(t)$, where $U_i(t)$ is the breathing waveform in tensor form. The inhalation flow rate ranges from 10 L/min to 60 L/min, representing the resting to exercise conditions (Robinson, Snyder, & Oldham, 2007). Accordingly, the breathing frequency varies from 15 to 60 times per min. For transient simulations, both idealized sinusoidal functions and realistic breathing waveforms have been employed as the airflow velocity B.C. at the mouth and nose openings (Haghnegahdar, Zhao, & Feng, 2019; Zhang & Kleinstreuer, 2002). If necessary, airflow temperature and relative humidity should be defined based on the environmental conditions that can be obtained from field data measurements.
(2) To define the inhalation conditions for both the PM and vapor/gas, exposure conditions must be obtained from the field data of aerosol characterization. Parameters required include:
- The diameter, density, and velocity for each particle inhaled;
- Particle orientations if the rotational motion will be solved for non-spherical particles, i.e.,
- Initial compositions of the multi-component droplets if condensation and evaporation effects will be modeled, the $Y_{s,ini}$.

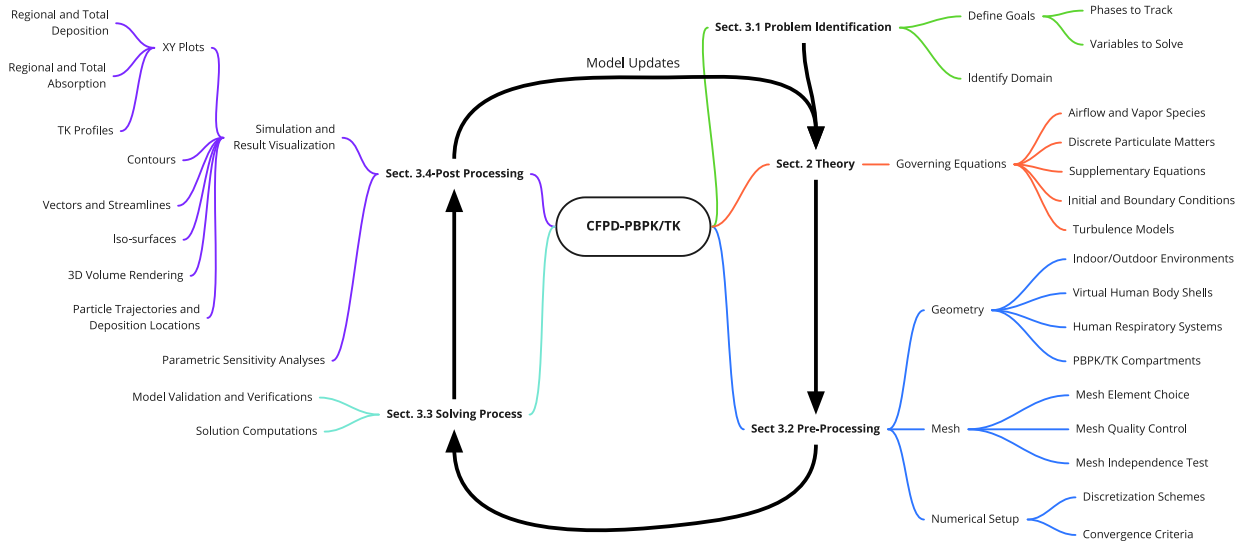

Fig. 5. Schematic of the CFPD-PBPK/TK simulation workflow.

- Vapor/gas concentrations or mass flow rates, i.e., $Y_s|_{mouth/nose} = Y(t)$ or $Q_i(t)|_{mouth/nose} = Q(t)$. $Y(t)$ and $Q(t)$ can be obtained from field data measurements.

2.2.5.2. Distal airway boundary conditions. Most of the human respiratory system geometries used in CFPD-PBPK/TK studies are incomplete and truncated at certain generations. Therefore, it is hard to obtain physiologically realistic values of airflow velocities or pressures at the truncated distal airway openings (see Fig. 4). With simplifications, commonly accepted distal airway B.C.s include uniform pressure/velocity outlets (Yin, Choi, Hoffman, Tawhai, & Lin, 2010) and mass flow rate distributionsobtained from experimental measurements (Worth Longest & Xi, 2008). It has been claimed that using uniform pressure/velocity outlets may not be physiologically realistic and will lead to noticeable differences in the airflow field predictions in human respiratory systems. Accordingly, utilizing experimental data, including 4D medical images, methods to estimate more physiologically realistic pressure or volumetric flow rate B.C.s have been developed (Oakes et al., 2014; Oakes, Shadden, Grandmont, & Vignon-Clementel, 2017; Yin et al., 2010; Yin, Hoffman, & Lin, 2009). Specifically, based on the radiological characteristics and volumetric changes of each lobe shown in 4D CT images, the regional ventilation conditions of the distal airways of different lobes can be estimated.

2.2.5.3. Airway wall boundary conditions. The internal walls of the human respiratory system are covered by mucus layers. Mucus layers serve to trap particulate matter (PM) carried by the inspiratory airflow and thereby performs a filtration function. Based on such a fact, 100% trapping wall B.C.s are widely used as particle deposition B.C. (Bui et al., 2020; Xi et al., 2016; Inthavong, 2020; Schroeter et al., 2019; Tian & Ahmadi, 2020; Tu et al., 2012). Specifically, if the distance between the spherical particle center and the airway wall is less than the particle radius, the particle is considered deposited.

To calculate vapor/gas absorption rates at the airway wall, both Dirichlet and Robin B.C.s have been applied in existing research efforts. Specifically, the Dirichlet B.C. can be given by:

$$Y_s|_{wall} = 0 \tag{24}$$

which implies the fast removal of vapor/gas with an infinite absorption rate.

However, the infinite absorption rate is not realistic. In contrast, the Robin B.C. (Keyhani, Scherer, & Mozell, 1997) is more realistic since it represents a limited absorption rate, but it needs more support from experimental measurements on the diffusion properties. The Robin B.C. for gas/vapor absorption can be given as:

$$\frac{\partial Y_s}{\partial n}|_{wall} + \Gamma_{s,w} \cdot Y_s|_{wall} = 0 \tag{25}$$

where n represents the normal direction of the airway surface, $\Gamma_{s,w}$ is the wall absorption coefficient which can be given by (Keyhani et al., 1997):

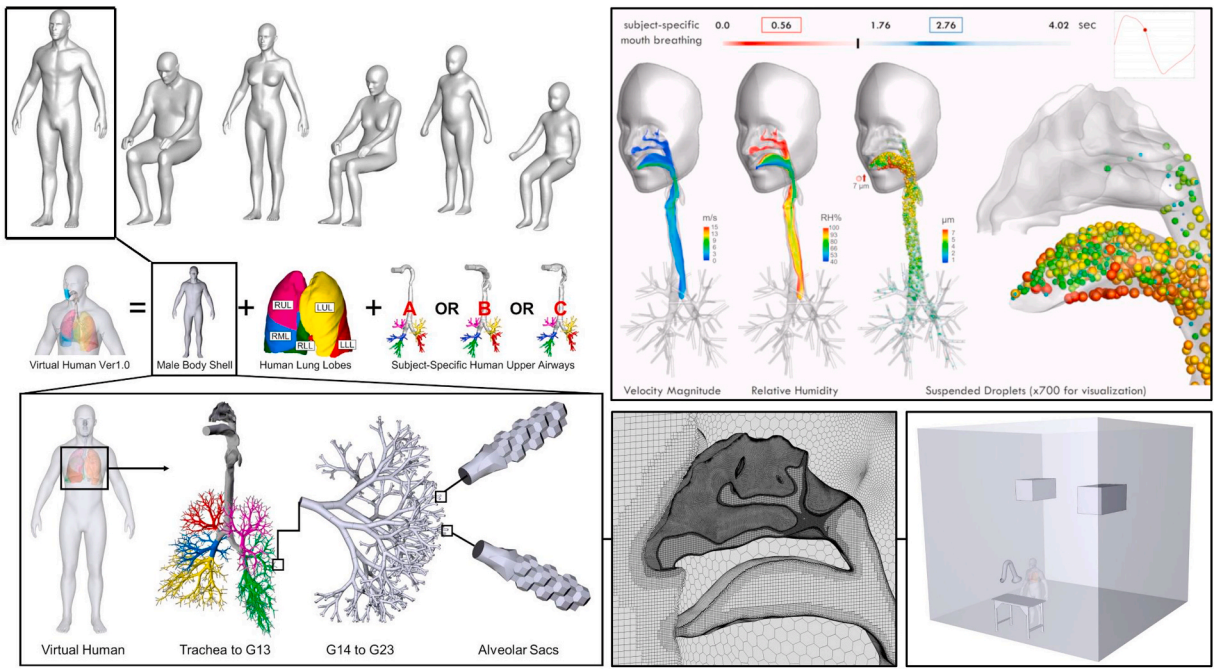

Fig. 6. The virtual ambient space and the virtual human system with a representative human respiratory system for Computational Fluid-Particle Dynamics (CFPD) simulations.

$$\Gamma_{s,w} = \frac{\widetilde{D}_{m,s}}{\widetilde{D}_{a-v,s} k_{H,s,a-m} H_m} \tag{26}$$

in which $\widetilde{D}_{a-v,s}$ and $\widetilde{D}_{m,s}$ are the vapor diffusivity in the air and the liquid mucus phase, respectively. H_m is the mucus thickness, which can vary from 8.3 μm in the trachea to 1.8 μm in the lower bronchioles (Asgharian et al., 2001; Hofmann & Sturm, 2004). $k_{H,s,a-m}$ is the equilibrium partition coefficient for a given contaminant molecule, which can be determined by Henry's law. Derivation of Eq. (25) can be found in (Keyhani et al., 1997).

In addition, the temperature at the airway wall usually is assumed to be the body temperature, i.e., 37 °C, and the relative humidity at the airway wall is assumed to be larger than 99% (Worth Longest & Xi, 2008). However, experimental results indicate that the relative humidities on the upper airway walls may be much lower than 99% due to the influence of dry air inhaled (Ferron, Oberdorster, & Henneberg, 1989; Ferron, Upadhyay, Zimmermann, & Karg, 2013). Therefore, using the idealized relative humidity B.C. may lead to unrealistic droplet size change dynamics and the resultant droplet deposition patterns. Research efforts have been done to enable a more realistic airway wall boundary condition, by modeling the convection over the mucus layer and the latent heat flux due to the evaporation of water vapor in the mucus (Chen et al., 2020; Yin et al., 2010). The schematic of the multi-layer airway boundary condition is given in (Chen et al., 2020; Yin et al., 2010).

2.2.6. *Initial conditions*

2.2.6.1. Initial conditions for CFPD simulations. The accurate and realistic temporal evolution variations of variables require reasonable initial conditions (I.C.s) to be given for CFPD simulations. Unless the simulation results of interest is steady-state, I.C.s must accurately reflect the conditions at time t = 0, e.g., the initial distributions of velocity, temperature, and pressure in the pulmonary airflow fields.

2.2.6.2. Initial conditions for PBPK/TK simulations. Since the generalized time-dependent PBPK/TK ODE, i.e., Eq. (12), is assumed to be only time-dependent, no B.C.s is needed but only I.C.s. Specifically, I.C.s needed are the initial concentrations C_T at t = 0, which can be calculated based on the deposition/absorption rates of the CFPD simulations.

3. Numerical method

Since the governing equations (see Section 2) are mostly non-linear partial differential equations (PDEs), which are not able to be solved analytically, numerical methods such as the finite volume method (FVM) (Pletcher, Tannehill, & Anderson, 2012) are employed to convert differential equations into a set of algebraic equations. The algebraic equations can then be solved numerically. The conversion requires the discretization of the computational domain, i.e., mesh generation (see Section 3.2.1), as well as the discretization of governing equations, i.e., approximating both spatial and temporal derivatives by finite differences derived using Taylor series expansion and/or Green Theorem (Pletcher et al., 2012). Numerical errors are inevitable during the above-mentioned computing process. Double precision solvers are preferable for the CFPD-PBPK/TK simulations.

To minimize the uncertainties of the CFPD-PBPK/TK simulation results, this section serves as a step-by-step tutorial for the readers without numerical modeling experience. It presents the details on how to set up numerical simulation cases using CFPD-PBPK/TK model with high credibility. The whole procedure is divided into four steps: problem identification, pre-process, solving process, and post-process (see Fig. 5). The following key substeps to guarantee the accuracy and reliability of the numerical model are emphasized in this section and Section 2, i.e.,

(1) Mesh independence test (see Section 3.2.1.2),
(2) Turbulence model selection (see Section 2.2.4),
(3) Convergence criteria (see Section 3.2.2.3), and
(4) Model validations and verifications (see Section 3.3.1).

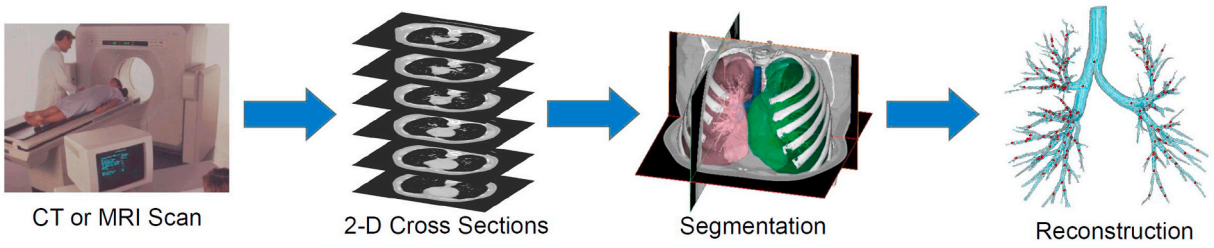

Fig. 7. Steps to reconstruct subject-specific human respiratory system geometries from CT/MRI scans.

3.1. Problem identification

Before running CFPD-PBPK/TK models, it is important to recognize the research problem and identify the system to simulate by answering the following questions:

(1) What is the goal of the CFPD-PBPK/TK simulations, and what are the processes of the aerosol dynamics need to be modeled, i.e., generation, ambient airborne transmission, inhalation, lung deposition, and/or systemic translocation?
(2) To quantitatively characterize the aerosol dynamics, what are the variables that need to be solved at where?
(3) Based on the processes that need to be modeled, what should the computational domain include? For example, should the computational domain include the ambient environment, virtual human body shell, and/or the human respiratory systems?
(4) According to the answers to (2) and (3), what and how many governing equations are needed to build the CFPD-PBPK/TK model to solve all the unknown variables and encompass the key physics and chemistry in the process (see Section 2 for the governing equations). To establish the governing equation system, more details need to be identified (see the questions listed in Section 2.1).
(5) What are the data needed in order to solve the governing equations identified in (4)? For example, what are the required initial conditions, boundary conditions, aerosol properties, etc.? Can they be obtained from experiments, or calculated using theoretical methods?

After all the above-mentioned questions are answered, the pre-processing can be started.

3.2. Pre-processing

Pre-processing includes steps to prepare geometry, mesh, and numerical setup before the start of the solving process.

3.2.1. Geometry and mesh generation

To accurately predict the airborne transmission, inhalation, and deposition of the aerosol from an ambient environment into the human respiratory system, the computational domain needs to be reconstructed with the following components, as shown in Fig. 6:

(1) Accurate indoor or outdoor spaces with realistic ventilation components and aerosol generation sources (Chen, Feng, Zhong, & Kleinstreuer, 2017; ; Feng et al., 2015; Feng et al., 2018; Haghnegahdar, Zhao, & Feng, 2019; Zhao et al., 2019);
(2) The virtual human with the respiratory system connected at the nostrils and mouth opening (Kuga et al., 2020; Zhao et al., 2019).

3.2.1.1. Geometry reconstruction of human respiratory systems. The human respiratory system contains the respiratory passage, lung, and respiratory muscles. For CFPD simulation, the reconstructed human respiratory systems should have the whole ventilation path containing mouth, nose, pharynx, glottis, larynx, trachea, bronchi, bronchioles (including terminal bronchioles, respiratory bronchioles, and alveoli) (Horsfield & Cumming, 1968). The path is divided into two functional zones. The respiratory zone is the region where gas exchange occurs, which includes respiratory bronchioles and alveoli; the conducting zone consists of all of the anatomical

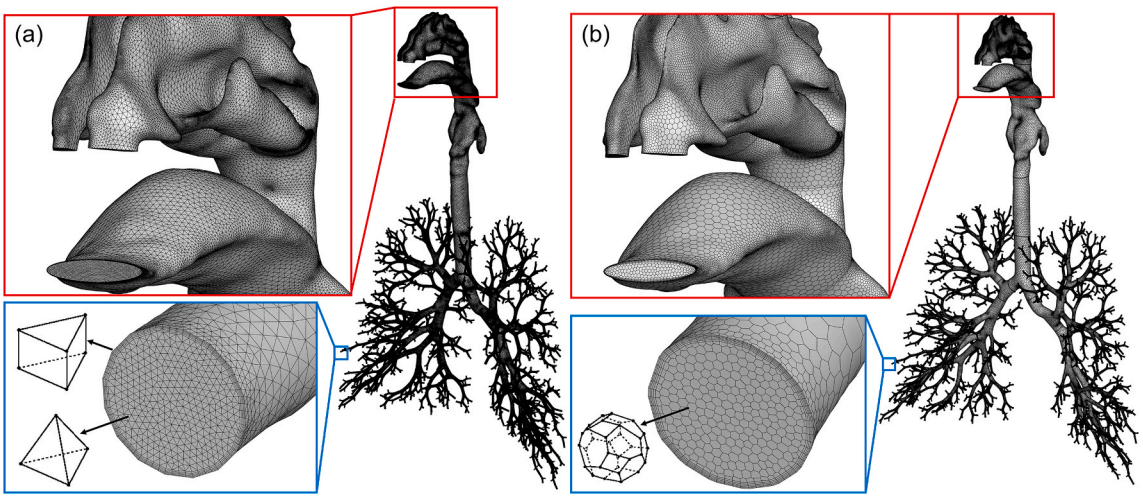

Fig. 8. Commonly used unstructured mesh elements for human respiratory systems: (a) tetrahedral mesh with prism layers, and (b) polyhedral mesh.

structures through which air passes before reaching the respiratory zone, i.e., mouth/nose to terminal bronchioles. Also, the human respiratory system can be divided into the upper airway and lower airway. The upper airway includes all structures above the glottis, while the lower airway is from the vocal cords to the alveoli. Another way of dividing human respiratory systems categories it into three parts (Kleinstreuer & Zhang, 2010), i.e., the extrathoracic region (i.e., nose, mouth, and throat), the tracheobronchial part (i.e., trachea, and bronchial tree), and the alveolar region (i.e., alveolar ducts and sacs).

Accurate and realistic human respiratory system models compose the necessary precursor for computational airflow and particle transport/deposition analyses. Instead of utilizing highly simplified idealized human respiratory system geometries (Wei, Byron, & Longest, 2014; Xi & Longest, 2007; Zhang, Finlay, & Matida, 2004), realistic subject-specific human airway models are more widely used nowadays with advances in imaging processing techniques and computational resources. To reconstruct subject-specific human respiratory systems, clinical image processing can be done in the following steps (see Fig. 7) (Lin, Tawhai, & Hoffman, 2013; Reynisson et al., 2015):

(1) Obtain a computer rendition using 3D imaging techniques, such as computerized tomography (CT) and magnetic resonance imaging (MRI). The files are usually in the digital imaging and communication in medicine (DICOM) data format.
(2) Perform segmentation to separate the respiratory system regions. The segmentation includes generating airway centerlines, cutting airway endings, generating lobes, and cleaning the geometry to a single-connected domain.
(3) The airway geometry then can be exported as Stereolithography (STL) format files for mesh generation as needed for computer modeling and simulations. Available image processing software packages for respiratory systems are Amira, Simpleware ScanIP, and Materialise Mimics.

In addition, open CT/MRI scanned data libraries are listed in the references (COPDGene, 2019; NBIA, 2019; Scans, 2020), which can be utilized to build the human respiratory system geometries with inter-subject variabilities in airway morphologies.

3.2.1.2. Mesh generation and independence test

3.2.1.2.1. Mesh generation. The airflow fields in the ambient environment and the human respiratory systems involve flows through complex geometries. To accurately predict such flow patterns, the computational domain must be discretized into small finite volume elements, i.e., mesh generation. As one of the essential aspects of CFPD simulations, appropriate mesh generation is vital for an accurate solution, faster convergence, and reduction of numerical diffusion. A numerically rigorous mesh generation process must guarantee the use of appropriate mesh element type, as well as the quality of the mesh elements.

3.2.1.2.2. Types of mesh elements. Three dimensional (3D) CFD meshes are either structured or unstructured, which are categorized by the mesh element connectivity to each other. For structured mesh generation, the 3D computational domain is discretized into hexahedrons (Chen, Kleinstreuer, Zhong, Feng, & Zhou, 2018; Feng, Kleinstreuer, Castro, & Rostami, 2016; Feng et al., 2015; Xi & Longest, 2007). Although structured mesh has several advantages compared with unstructured mesh such as a high degree of mesh quality control, better convergence, and less computational time (Pletcher et al., 2012; Tu et al., 2012), it is used less in recent computational lung aerosol dynamics research because of the following reasons:

(1) The generation of structured mesh for the complex geometries of subject-specific human respiratory systems is challenging and time-consuming. Therefore, with more preferences on using subject-specific airway geometries, using structured mesh is not convenient.
(2) With the increase in computational resources, the extra computational time using unstructured meshes (see Fig. 8 (a) and (b)) are more affordable.

Unstructured meshes for respiratory systems are used to only consist of tetrahedrons, pyramids, and prisms with irregular connectivity to their neighbor mesh elements (see Fig. 8 (a)). Although unstructured mesh can approximate almost any arbitrarily shaped geometry in great detail, the unstructured mesh will produce more truncation error when calculating flow gradients at cell faces using the cell center variable values. Such sacrifices using unstructured mesh also apply on polyhedral mesh elements, and poly-hexcore mesh strategy discussed below.

With the unstructured mesh generation techniques developing in the past decades, polyhedral meshes are more preferred for the computational lung aerosol dynamics study (Feng et al., 2020; Haghnegahdar, Zhao, & Feng, 2019; Shang, Dong, Tian, Inthavong, & Tu, 2019). An example of the polyhedral mesh is shown in Fig. 8 (b). Compared with tetrahedron based mesh, polyhedron based mesh has the following advantages:

(1) Enhanced computation efficiency for cases with less mesh element numbers,
(2) Better stability and convergence,
(3) More accuracy due to enhanced cell connectivity, and
(4) Significantly lower average inverse orthogonal quality, i.e., better mesh quality control.

Specifically, polyhedral elements have more neighbor cells than tetrahedral elements, so gradients can be better approximated than with tetrahedral elements for better convergence. However, as of the date of this publication, the polyhedral mesh is not compatible with the dynamic mesh method to model the airway expansion and contraction motion (see Section 4.2.1).

When both the ambient environment and human respiratory systems need to be modeled (Kuga et al., 2020; Zhao et al., 2019), the geometric dimension scales in the flow domains vary drastically. The poly-hexcore mesh can be then employed to achieve smooth transitions from the environmental to pulmonary characteristic length, i.e., from meters to millimeters (Zhao et al., 2019). Specifically, the mosaic technology (Zore, Caridi, & Lockley, 2020) was used to fills the bulk region with octree-based hexahedrons and the near-wall boundary layer with poly-prisms, and connect the two meshes with general polyhedrons. Compared with the tetrahedral and polyhedral mesh, the poly-hexcore mesh has fewer and better-quality mesh elements, requiring less memory and better computational efficiency, as well as slightly better parallel scalability on high-performance computers (Zore et al., 2020; Zore, Parkhi, Sasanapuri, & Varghese, 2019).

As shown in Fig. 8 (a) & (b), near-wall prism layers are usually generated and refined to guarantee that the thickness of the first prism layer satisfies y^+ and the first near-wall cell height requirements when employing different turbulence models (see Section 2.2.4), where y^+ is the dimensionless wall distance (Menter, 1994; Menter, Langtry, & Völker, 2006; Florian R.). Compared with the isotropic tetrahedral elements, anisotropic prism layers are computationally efficient to resolve the full resolution of the boundary layer and the high gradients along with the normal directions to the walls. Inappropriate y^+ may lead to inaccurate predictions of the pressure drop and the transition onset location of the airflow regime between laminar and turbulence, especially in human respiratory systems.

3.2.1.2.3. Mesh generation procedure and available software. Good mesh generation procedures should be able to fill the complex computational domain with high-quality surface meshes and volume meshes. Usually, the mesh generation procedure should follow the steps below:

(1) Import geometries into the mesh generation software,
(2) Define and mesh the edges with appropriate mesh edge lengths,
(3) Define and mesh the surfaces with appropriate surface mesh element sizes, and
(4) Fill the 3D computational domain using volume mesh elements.

It is worth mentioning that in some mesh generation software, Step 2 is not necessary. Widely used meshing software packages for airways are Fluent Meshing (ANSYS Inc., Canonsburg, PA), ICEM CFD (ANSYS Inc., Canonsburg, PA), and open-source packages such as blockMesh, SnappyHexMesh, and cfMesh.

3.2.1.2.4. Mesh quality control and refinement. Low mesh quality and refinement will cause inaccurate solutions and slow convergence. Guidelines are listed as follows to facilitate the readers to pay attention to overall critical principles to generate meshes with good quality, necessary local refinements, and an optimized balance between computational accuracy and efficiency.

(1) Different measures of mesh quality should be used for different types of mesh elements. Commonly used measures are skewness, smoothness, aspect ratio, and orthogonal quality (Garimella, Kim, & Berndt, 2014; Paoletti, 2002; Tu et al., 2012). Specifically,
   - For hexahedral mesh, skewness should not exceed 0.85;
   - For tetrahedral mesh, skewness should not exceed 0.9;
   - For polyhedral mesh, the orthogonality should be as large as possible;
   - Mesh element aspect ratio should be close to 1.0, when the flow is multi-directional; and
   - Mesh elements can be stretched along the fully-developed direction, e.g., the mainstream direction in the boundary layer.
(2) For localized mesh refinement, the mesh density should be sufficiently high to capture local flow features. For example, the near-wall mesh should be finer to resolve the boundary layer flow field, because of the high gradients along the normal direction to the wall. Local variations in cell size, i.e., the spacing ratios between adjacent cells, should be less than 120%.

Indeed, numerical errors can be significant if the mesh is coarse, the skewness is high, the volume change in adjacent cells is significant, the aspect ratio is large, and the near-wall mesh is not appropriately refined, etc.

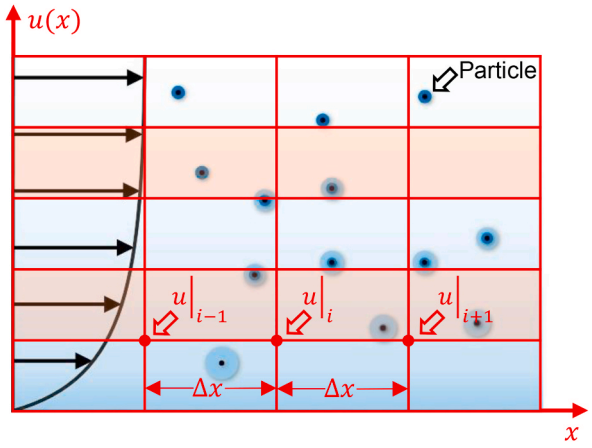

Fig. 9. Illustration of spatial discretization of the 2D airway using finite differences into nodal values.

Table 3
Available data sources for model V&V.

Submodel	Description	Geometry	Data Sources
LES	3D laminar-to-turbulence airflows	Constricted tube, and subject-specific mouth-to-G6 geometry	(Ahmed & Giddens, 1983a, 1983b; Banko et al., 2015; Bernate et al., 2017; Jalal et al., 2020)
	Steady and transient laminar	Single bifurcation	(Lieber & Zhao, 1998; Zhao & Lieber, 1994)
DPM	Steady inspiratory particle distributions, deposition patterns, and efficiencies	Double bifurcation airway model, oral airway model, nasal cavity, curved bend, and a tracheobronchial tree	(Cheng et al., 1996; Heyder, Gebhart, Stahlhofen, & Stuck, 1982; Hofmann, Bolt, Sturm, Fleming, & Conway, 2005; Kelly, Asgharian, Kimbell, & Wong, 2004; Kim & Fisher, 1999; Kim & Jaques, 2004; Kwok et al., 2020; Schiller, Gebhart, Heyder, Rudolf, & Stahlhofen, 1988; Smith, Cheng, & Yeh, 2001; Stahlhofen, Gebhart, & Heyder, 1981; Stahlhofen, Rudolf, & James, 1989; Su, Chen, Bezerra, & Wang, 2019; Sul et al., 2019)
Species Transport	Soluble gas uptake	A single straight tube and a network	Kaye and Schroter (1993)
	Odorant deposition fractions	Nasal airway model	(Hu, Ben-Jebria, & Ultman, 1994; Rigas, Catlin, Ben-Jebria, & Ultman, 2000)
Mucus VOF	Mucus moving velocity	An annular tube	((Kim, Greene, Sankaran, & Sackner, 1986)
Airway Deformation	Airway pressure and average meniscus velocity during airway opening	Asymmetric, collapsed, tethered airway model	(Perun & Gaver, 1995, 1995b)
	Lung volume change	PFT and 4D CT data	(Bates & T., 2009; Bobbio et al., 2005; de Camargo, Justino, de Andrade, Malaguti, & Dal Corso, 2011; Fan, Xia, Guan, Zhang, & Liu, 2014; West, 1979)

3.2.1.2.5. Mesh independence test. Since all derivatives in the governing equations will be approximated using truncated Taylor series expansions, which causes the truncation error (Ferziger & PERIĆ, 1996; Pletcher et al., 2012). The truncation error is proportional to the mesh size and time step. To minimize the truncation error, the mesh size should be as small as possible. However, an overly refined mesh is not preferred since it will increase in round-off error (Ferziger & PERIĆ, 1996; Pletcher et al., 2012) and computational time. To address such a dilemma, the mesh independence test must be carried out to identify the optimized level of mesh refinements for accurate numerical simulation results with affordable computational time. Steps to perform the mesh independence test are:

(1) Generate an initial and relatively coarse mesh (Mesh 1) and run CFPD simulations. Three conditions must be satisfied for the simulation using the initial mesh:
   - The residual of the convergence criteria should be at least 10^{-4}.
   - Several monitor points in the computational domain should also be created, and variable values at those points should be steady.
   - The mass imbalances should be lower than 1%.
   - If the above conditions cannot be met, regenerate a finer mesh and repeat it.

(2) Once the above conditions are satisfied using the initial mesh (Mesh 1), refine the mesh and generate multiple meshes with different mesh element sizes, i.e., Mesh 2, Mesh 3, Mesh 4, etc. The reduction of the mesh size should be around 1.3 to 2.0 times between two meshes with consecutive numbers. Using the same convergence criteria and other conditions in Step 1, run simulations using different meshes with the same numerical setup, and record all simulation results.

(3) Compare the numerical results using different meshes. If the difference between the numerical results is lower than the allowable tolerance, with meshes further refined, then it can be concluded that the numerical results are independent of the mesh. Then the least refined mesh will be the final mesh to be used for the CFPD simulations, which can generate the mesh independent simulation results with the best computational efficiency.

(4) The mesh topology should be further refined until the mesh independence described in Step 3 can be achieved.

3.2.2. Numerical setup

As mentioned in Sections 2.1 & 2.2, the appropriate governing equation system should be first established based on the problem identification, and be solved using numerical methods. The overall steps are listed as follows, with some overlaps compare with Section 3.1:

(1) Selection of dependent and independent variables,
(2) Choice of model type and modeling approach,
(3) Determination of basic equations plus initial and/or boundary conditions (see Section 2.2.5),
(4) List of assumptions and postulates for the derivation of modeling equations,
(5) Development of submodels to gain closure, including turbulence model selection (please see Section 2.2.4),
(6) Selection of appropriate numerical methods, discretization schemes, time steps, convergence criteria, and parameter ranges, etc.,
(7) Model validations and verifications (e.g., experimental data sets, flow visualization, and exact analytical solutions).

3.2.2.1. Discretization schemes. To solve the partial differential governing equations, the temporal and spatial derivatives are approximated by their finite differences. Through the finite difference approximations, the differential equations can be converted to sets of algebraic equations which are solved for the unknowns at mesh cell centers, face centers, and mesh nodes. The discretization is

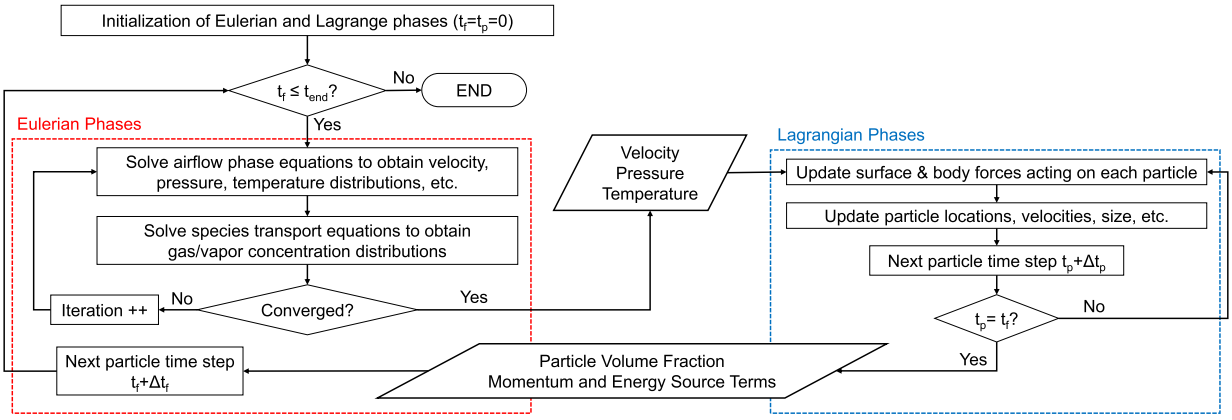

Fig. 10. The solving process using the Euler-Lagrange method with the coupling mechanisms between Eulerian and Lagrangian phases.

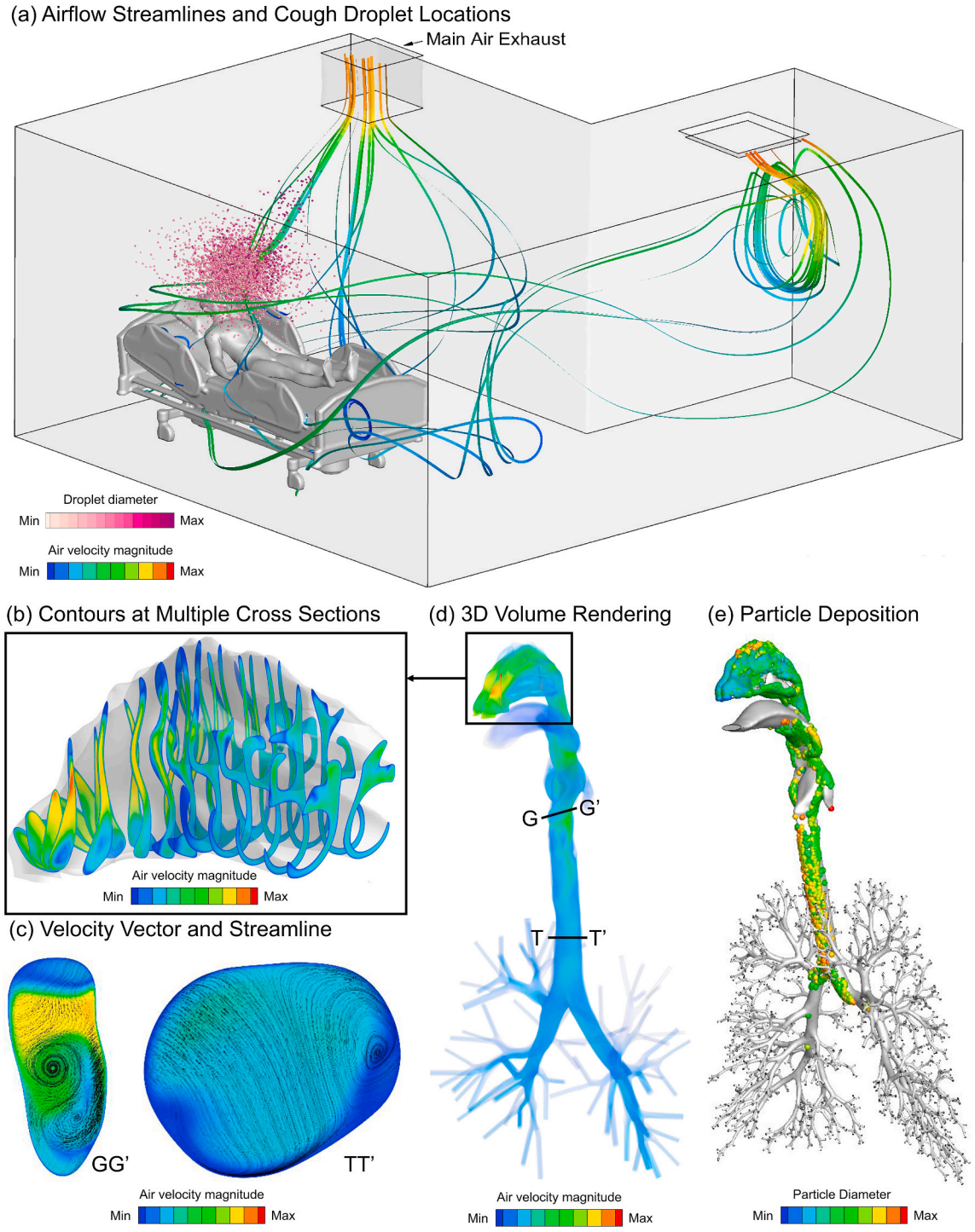

Fig. 11. Examples of 3D visualizations of CFPD-PBPK/TK simulation results using different post-processing techniques: (a) airflow streamlines and cough droplet locations emitted by a virtual patient in a patient room with certain ventilation conditions; (b) Velocity magnitude contours at multiple cross-sections in human nasal cavity geometry; (c) In-plane velocity vectors and streamlines at the vocal fold and the bottom of the trachea; (d) 3D volume rendering colored by air velocity magnitude in a human respiratory system; and (e) particle deposition locations colored by particle diameter.

demonstrated by the finite difference method (FDM) in this section. Specifically, using spatial derivative $\frac{\partial u}{\partial x}$ and $\frac{\partial^2 u}{\partial x^2}$ as examples, it can be replaced by different discretization schemes. For example,

$$\left.\frac{\partial u}{\partial x}\right|_i \approx \frac{u|_{i+1} - u|_i}{\Delta x} \tag{27}$$

$$\left.\frac{\partial u}{\partial x}\right|_i \approx \frac{u|_i - u|_{i-1}}{\Delta x} \tag{28}$$

$$\left.\frac{\partial u}{\partial x}\right|_i \approx \frac{u|_{i+1} - u|_{i-1}}{2\Delta x} \tag{29}$$

$$\left.\frac{\partial^2 u}{\partial x^2}\right|_i \approx \frac{u|_{i+1} - 2u|_i + u|_{i-1}}{\Delta x^2} \tag{30}$$

Eqs. (27)–(30) represent forward difference, backward difference, the central difference schemes for 1st-order derivative, and the central difference scheme for 2nd-order derivative, respectively (Pletcher et al., 2012). In Eqs. (27)–(30), the subscript i implies different nodal positions (see Fig. 9). The algebraic equation system then can be solved iteratively. Basic steps are listed as follows:

- **Step 1:**Divide the spatial and temporal region into smaller regions by placing grid points (nodes) on the line, surface, volume, etc.
- **Step 2:** Unknown dependent variable (as a function) can be expanded in Taylor's series about the value at a nodal point.
- **Step 3:** Rearrange with different expansions and obtain the approximation for the derivative.
- **Step 4:** Replace the differential equation with a set of equations at all nodal points:
  - Each algebraic equation holds for the region close to just one node.
- **Step 5:** Solve the system of algebraic equations using
  - Direct Method
  - Iterative Method

More details of the finite volume method (FVM) can be found in (Pletcher et al., 2012).

It is worth mentioning that the discretization schemes shown in Table 3 can also be applied on the translation equation (see Eq. (6)) for tracking the Lagrange phases. The coupling between solving Eulerian phases and Lagrangian phases are shown in Fig. 10.

3.2.2.2. Convergence criteria. CFPD-PBPK/TK numerical simulations involve checking for convergence of the iterative solving process of the algebraic equation systems (Pletcher et al., 2012). Convergence is a measure of the conservation of multiphase flow properties, which can be quantitatively assessed by progressively calculating the imbalances that originate from the initial and boundary conditions. These imbalances are the residuals (Pletcher et al., 2012). Residuals need to be monitored closely to ensure that it has a trend to decrease, which implies the removal of imbalances leading to a converging solution, as opposed to the possible accumulation of numerical errors leading to inconvergence and even divergence. Convergence is achieved when the residuals satisfy certain

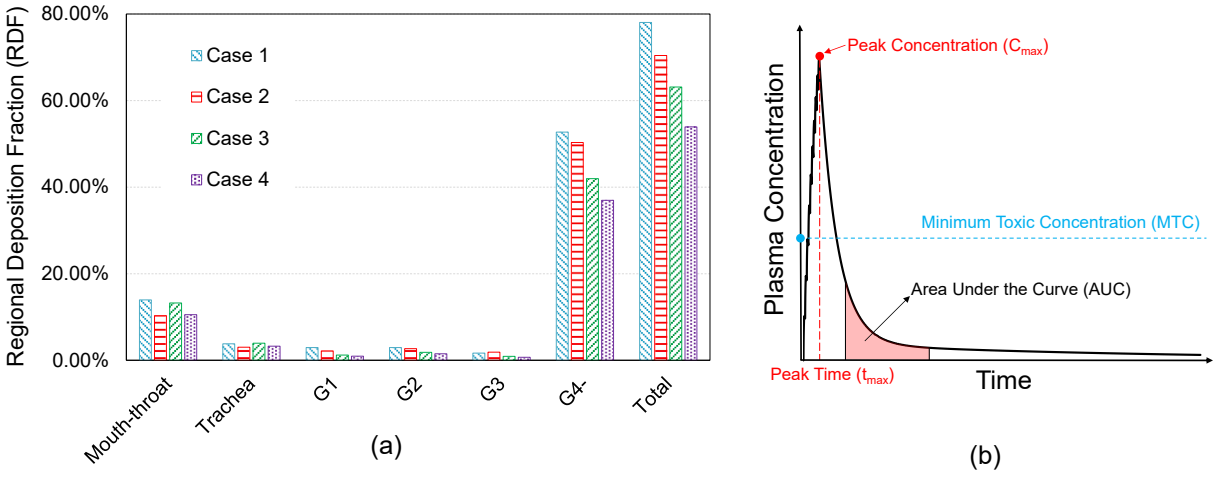

Fig. 12. Examples of 2D plots of CFPD-PBPK/TK simulation results for quantitative analyses: (a) deposition fractions (DFs) in different pulmonary regions, and (b) plasma concentration vs. time for toxicokinetic (TK) analyses.

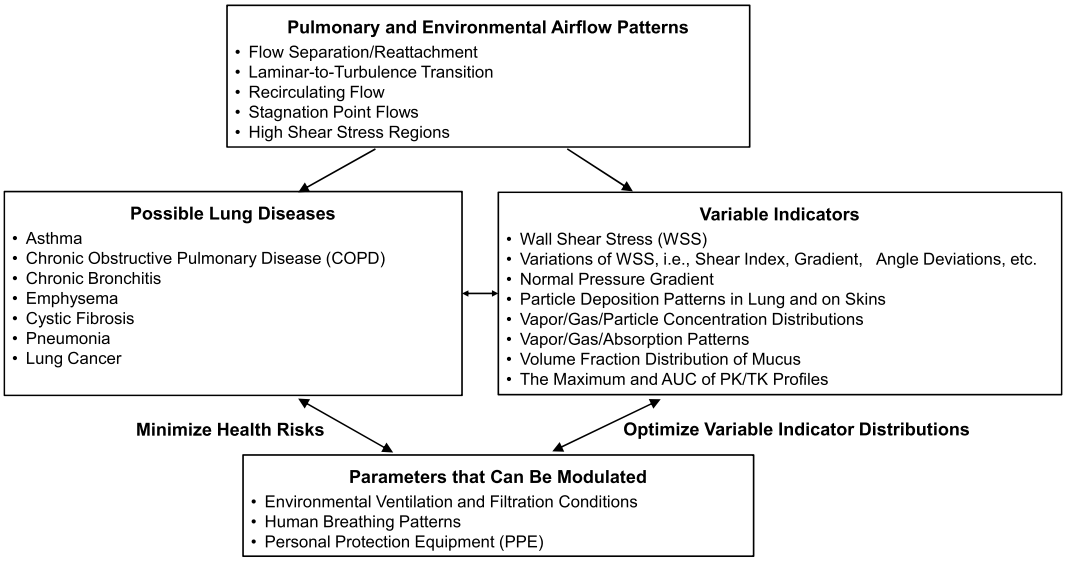

Fig. 13. Flowchart of parametric sensitivity analysis strategies for computational lung aerosol dynamics research using CFPD-PBPK/TK models.

convergence criteria that can be preset by controlling parameters of the iterative solvers. Residuals should be lower than 10^{-4} for continuity and momentum equations, while lower than 10^{-6} for scalar transport equations such as temperature and concentration. Besides examining the residuals, variables at the monitoring point in the computational domain can also be selected to confirm the convergence of the numerical simulations.

3.2.2.3. Time step size selection. There are two aspects of the CFPD-PBPK/TK simulation results that can be influenced by the time step size, i.e., stability and accuracy. Depending on the mesh size, the type of governing equations, and the discretization schemes, the airflow time step size should be lower than specific values to satisfy the stability conditions. Details of the stability analysis to determine the time step size can be found in (Pletcher et al., 2012). Considering the accuracy, which is similar to the mesh independence test (see Section 3.2.1.2) , time step independence tests for both airflow and particle should also be performed for transient simulations to ascertain that the airflow field and particle trajectories are insensitive to the further refinement of the time step sizes. Large time step size may introduce large temporal advancement, lack of iterative convergence, and inaccurate predictions.

3.3. Solving process

3.3.1. Model validations and verifications

Other than the independence tests discussed above, the model validation and verification (ASME V&V 40 Subcommittee on Verification and Validation of Computational Modeling for Medical Devices, 2018) is also an essential process to:

(1) Justify the correctness of the fundamental equations employed to govern the multiphase flow dynamics;
(2) Assess the numerical uncertainties caused by the assumptions and simplifications made in the computational model.

As a widely accepted validation and verification procedure, scientists usually strictly follow the ASME Verification & Validation 40 Standard (ASME V&V 40 Subcommittee on Verification and Validation of Computational Modeling for Medical Devices, 2018) to establish the credibility of the CFPD-PBPK/TK model. Specifically, model validations and verifications for the CFPD models employed by the author's research group are divided into five levels by comparing:

(1) Transitional airflow field (Ahmed & Giddens, 1983a, 1983b; Banko et al., 2015; Bernate et al., 2017; Jalal, Van de Moortele, Amili, & Coletti, 2020);
(2) Particle translational and rotational motions and deposition data (Y Feng & C Kleinstreuer, 2013; Yu Feng & Clement Kleinstreuer, 2013; Feng & Kleinstreuer, 2014; Feng, Kleinstreuer, et al., 2016; Feng et al., 2015; Feng, Zhao, Chen, & Lin, 2017; Feng et al., 2018; Haghnegahdar et al., 2018; Haghnegahdar, Zhao, & Feng, 2019);
(3) Droplet size change dynamics due to condensation and evaporation (Chen et al., 2018; Feng, Xu, et al., 2016; Feng et al., 2015; Feng et al., 2020; Haghnegahdar, Zhao, & Feng, 2019);
(4) Airway deformation displacements (Zhao et al., 2020);
(5) Concentration time profiles in plasma and other organs (Corley et al., 2015; Haghnegahdar et al., 2018; Haghnegahdar, Zhao, & Feng, 2019).

The overall rule of the validation and verification (V&V) is that, any supplementary equations that are introduced into the CFPD-PBPK/TK model need to be validated and/or verified. For example, the V&V strategy for non-spherical particles, i.e., fiber-like particles, should focus on not only their deposition data but also their specific rotational motion validations (Y Feng & C Kleinstreuer, 2013; Islam et al., 2019; Tian & Ahmadi, 2020). The same V&V strategy should be applied for size change dynamics of multicomponent particles and droplets. Both their deposition and their diameter changes should be validated with experimental measurements. For transitional airflow field validations, it is highly preferred to compare 3D flow field in anatomically accurate replicas of human respiratory systems (Banko et al., 2015; Jalal et al., 2020). Some of the data sources for V&V are listed in Table 3, categorized by submodels.

3.3.2. Commercial vs. open-source CFD solvers

3.3.2.1. Commercial software: ANSYS Fluent. Commercial CFD packages that are widely used for computational lung aerosol dynamics are ANSYS Fluent and CFX (ANSYS Inc., Canonsburg, PA) (Inthavong et al., 2013; Longest et al., 2012; Tian et al., 2012; Xi & Longest, 2007; Zhao et al., 2019), and STAR-CCM+ (CD-Adapco Ltd, Plano, TX) (Collier, Wild, Oates, & Chung, 2013; Han, Hirahara, & Yoshizaki, 2016; Kadota et al., 2020; Taherian, Rahai, Gomez, & Waddington, 2014; Taherian, Rahai, & Waddington, 2011). The use of commercial solvers, e.g., ANSYS Fluent (ANSYS Inc., Canonsburg, PA), will significantly facilitate the simulation process. For research, using commercial solvers has the benefit of utilizing existing and well-validated advanced codes and modeling platforms using the same commercial software platforms, and facilitate the coupling between multiple submodels. Compared with open-source solvers or in-house programming, using commercial software may have fewer customization capabilities, but faster model development using robust commercial modules. However, learning CFPD-PBPK/TK model via commercial CFD solvers may make the researchers without CFD background lack of firm grasp of underlying numerical concepts and understanding how converged and accurate CFPD solutions are obtained due to the lack of fundamental training of CFD code development (Nijdam, 2013).

3.3.2.2. Open-source software: OpenFOAM. Considering the high license fee of commercial CFD packages, developing CFPD-PBPK/TK models using available open-source packages such as OpenFOAM® is a feasible option (Asgari, Lucci, & Kuczaj, 2019; Cui & Gutheil, 2011; Cui & Gutheil, 2018; Frederix et al., 2018; Myers, 2017; Vaish, Kleinstreuer, Kolanjiyil, Saini, & Pillalamarri, 2016). The most recent developed open-source CFD code based on OpenFOAM® is AeroSolved™ (www.aerosolved.com), which can simulate the generation, transport, and deposition of aerosol mixtures (Asgari et al., 2019; Frederix et al., 2018). An advantage of OpenFOAM® over commercial solvers is the capability of parallel processing. OpenFOAM® uses an open-source Message Passing Interface (MPI) tool, i.e., Open MPI, which can enable simulations using as many processors as the user has at its disposal. Commercial software allows parallel run only on a limited number of cores. However, OpenFOAM® is possibly unwieldy to use for the end users (e.g., toxicologists, regulators, clinicians, etc.), who may not be experienced with C++ and/or Linux.

3.4. Post-processing

3.4.1. Types of graphics

CFPD-PBPK/TK simulations have the capability to generate numerous "good-looking" images and animations. However, those beautiful and sophisticated graphics are meaningless if analysis and discussion based on the results are not insightful. To fully utilize the advantage of numerical simulation results and provide precise interpretations of the numerical solutions, different types of visualizations can be used for the preparation of meaningful graphics, such as XY plots, contours, streamlines, vectors, 3D volume rendering, and particle locations and deposition patterns (see Figs. 11 and 12 for examples). Different variables can be visualized to present the localized airflow field and aerosol dynamics using different types of graphics. For example, velocity, pressure, shear stress, turbulence intensity, and vapor concentration can be visualized as color-coded vectors and/or contours to display the full resolution that the CFPD-PBPK/TK model is able to explore. As integral parameters, regional and total particle deposition, vapor absorption, as well as the concentration-time profiles in plasma can be visualized using XY plots (Haghnegahdar et al., 2018; Haghnegahdar, Zhao, & Feng, 2019; Haghnegahdar, Zhao, et al., 2019). In addition, a potentially powerful display of transient CFPD results is animated movies. Available post-processing software includes CFD Post, Ensight, Tecplot, Paraview, etc.

3.4.2. Parametric sensitivity analyses strategy

Novel insight and enhanced understanding of the lung aerosol dynamics must be extracted from the unique features in all visualized results, instead of describing what can be observed from the graphs only. To achieve such goals, parametric sensitivity analyses, and unique ways of plotting the research results can be employed. Fig. 13 shows the flowchart summarizing the parametric sensitivity analysis strategy for lung aerosol dynamics found in existing publications (Dong, Ma, et al., 2018; Feng et al., 2020; Frederick et al., 2002; Inthavong et al., 2013; Kleinstreuer & Feng, 2013; Kuga et al., 2020; Kuga et al., 2018; Longest & Oldham, 2006; Shimazaki, Okubo, Yamamoto, & Yoshida, 2009; Tian et al., 2012; Tian et al., 2016; Xi & Longest, 2007; Zhao et al., 2019). The goal of parametric sensitivity analyses is to understand the fundamental science of particular aerosol transport and translocation dynamics, and find solutions to minimize the health risks due to the exposure via modulating specific environmental parameters and human factors.

Possible observations and insightful analysis on the patterns flow field, gas/vapor absorption, particle deposition, and TK profile are discussed below.

3.4.2.1. Airflow patterns. Due to the small sizes of the inhaled PM and gas/vapor molecules, they can follow the airflow well during

their transport in human respiratory systems. Therefore, understanding the airflow patterns is essential to understand the underlying physics that resulted in distinguished PM and gas/vapor fates. Normalized variables, i.e., velocity, secondary airflow intensities, turbulent intensity distributions, and wall stress distributions, can be studied during the breathing cycles. Expected pattern shifts of the Dean flow and swirl flow can be quantified. Helicity and other indicators can be used to visualize vortex structures and vortex shedding. For example, turbulence intensity (TI) can be a good indicator on local and regional turbulence dispersion effects on particle transport. High TI can lead to more dispersed particle deposition patterns and more even gas/vapor absorptions in a certain region. Additionally, the laryngeal jet effect will lead to distinguished particle deposition patterns in the trachea and first bifurcation due to the strong inertial impaction effect induced by the high-velocity streams (Feng et al., 2018). Furthermore, to quantify the changes in the degree of swirl, the Swirl number (S_0) [116] can be compared. To quantify the alteration in airflow unsteadiness, Womersley numbers (Wo) [117] can be employed. With the above mentioned dimensionless numbers and particle deposition patterns, the relationships between the particle mixing effect and the resultant deposition patterns from a microscopic view can be generated. Insights can be also generated with emphasis on how the airflow pattern shifts resulted from the airway deformation influence the local particle mixing, distributions, and depositions. To quantify the differences in particle mixing, distribution, and deposition, variables will be plotted and compared, e.g., (a) deposition fraction (DF) *vs.* particle Stokes number (St); and (b) particle Reynolds numbers (Re_p) at different cross-sections *vs.* St, Wo, and S_0. Different depositions can also indicate the dominancy of different deposition mechanisms, i.e., inertial impaction, gravitational sedimentation, and diffusion.

3.4.2.2. Regional particle depositions. XY plots can be used to summarize the quantitative relationships between aerosol fates and exposure conditions. For example, as shown in Fig. 12 (a), regional depositions can be visualized and compared associated with different exposure conditions, i.e., case numbers. The regional deposition of PM in human respiratory systems can be quantified in terms of the deposition fraction (DF), deposition efficiency (DE), and deposition enhancement factor (DEF). These three parameters can be defined as:

$$DF = \frac{\text{Number of deposited particles in a specific region}}{\text{Number of particles entering from the mouth/nose inlet}} \tag{31}$$

$$DE = \frac{\text{Number of deposited particles in a specific region}}{\text{Number of particles entering this region}} \tag{32}$$

$$DEF = \frac{DE_i/S_i}{\sum_{i=1}^{n} DE_i \Big/ \sum_{i=1}^{n} S_i} \tag{33}$$

where S_i is the area of the local wall face (i), n is the number of wall faces in a specific airway region, and DE_i is the local deposition efficiency on local wall face (i). High DEF-values indicate "hot spots" which is the location where particles accumulate the most.

3.4.2.3. Toxicokinetic (TK) profiles. As the direct quantitative evidence for potential health risks, toxicokinetic (TK) profiles such as plasma concentrations and organ concentrations (see Fig. 12 (b)) can be used to evaluate the exposure risks and analyze the relationships between the exposure conditions and the toxicodynamic (TD) responses. Specifically, several parameters of the TK profiles can be used for quantitative analysis. Using plasma concentration profile as an example (see Fig. 12 (b)), it can explicitly quantify the distribution of exogenous chemicals in the inhaled aerosols via the blood circulation, and their final deposition by ways of biotransformation and excretion. As mentioned earlier, the basic toxicokinetic (TK) mechanisms are absorption, distribution

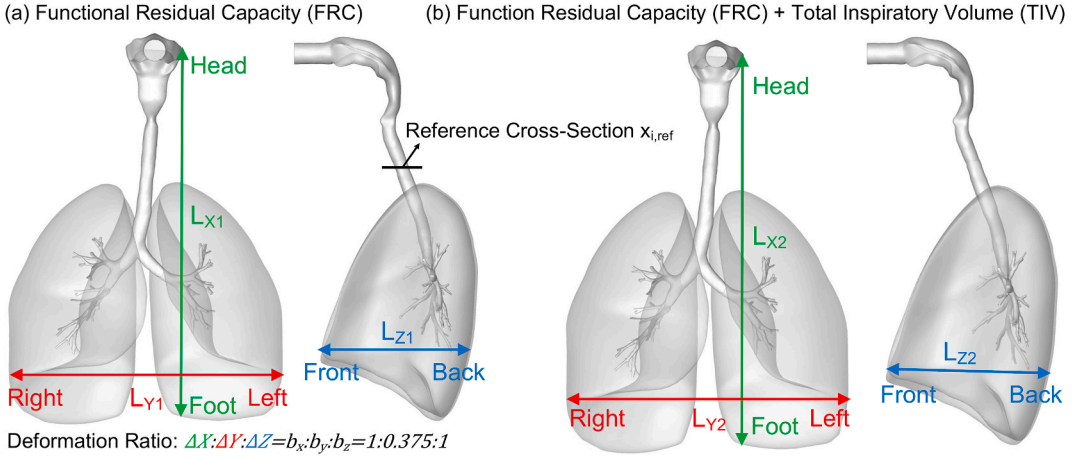

Fig. 14. Illustration of the airway deformation kinetics in the selected subject-specific human respiratory system.

metabolism, and excretion (ADME) (Klaassen & Amdur, 2013). Several parameters of the concentration profile can be used to evaluate the potential health risks. For example, the area under the curve (AUC) is a useful metric to determine the total toxicant exposure across certain time durations, the peak concentration (C_{max}) is an indicator of the maximum exposure risk compared with the minimum toxic concentration value (MTC), and the elimination half-life $T_{1/2}$ can be used to quantify the persistence of a toxicant following discontinuation of expoxure (Klaassen & Amdur, 2013). The chemical concentration profiles vs. time in organs and tissues can be also used to understand the dynamics of a toxic event, i.e., the onset and degree of toxicity, the accumulation of a chemical in the whole body, etc.

4. Challenges and outlook

4.1. Assumptions and simplifications of the current CFPD models

Although computational research efforts have been made to develop accurate and realistic lung dosimetry models (Dong, Ma, et al., 2018; Feng, Marchal, Sperry, & Yi, 2020; Frederick et al., 2002; Haghnegahdar et al., 2018; Haghnegahdar, Zhao, & Feng, 2019; Haghnegahdar, Zhao, et al., 2019; Inthavong et al., 2013; Kleinstreuer & Feng, 2013; Kuga, Ito, Chen, Wang, & Kumagai, 2020; Kuga et al., 2018; Longest & Oldham, 2006; Shimazaki, Okubo, Yamamoto, & Yoshida, 2009; Tian et al., 2012; Tian et al., 2016; Xi & Longest, 2007; Zhao, Feng, Bezerra, Wang, & Sperry, 2019), existing CFPD and PBPK/TK based computational models are developed with simplifications which limit their physiological realisticity. The assumptions and simplifications are summarized as follows:

(1) Static airway assumption negates the modeling capabilities of the effect of realistic airway deformation on inhaled transport and deposition;
(2) Incomplete 3D pulmonary airway geometries inhibit predictions of the physiologically realistic whole-lung deposition data under full breathing cyclic waveforms;
(3) 100% trapping wall boundary conditions disables modeling of disease-specific mucus movement and clearance of inhaled PM driven by cilia;
(4) Negligence of inter-species and inter-subject variabilities limit the statistical robustness of conclusions drawn from CFPD modeling results to represent a sub-population group.
(5) One-way coupling between the pulmonary airflow and carried particles neglects both the influence of the particle presence on the airflow pattern shifts and the particle-particle interactions.

4.2. Research efforts for developing the next-generation virtual lung model

To address the challenges mentioned above and focus on developing a next-generation virtual lung model, research efforts have been initiated and summarized as follows:

4.2.1. Build elastic airway models

It has been demonstrated that the transient airway deformations can influence the accuracy of the particle transport and deposition in human respiratory systems (Zhao et al., 2020). Thus, recovering the real-time anisotropic lung deformation is necessary, for the precise predictions of PM deposition and gas absorption (De Groote, Wantier, Chéron, Estenne, & Paiva, 1997; Plathow et al., 2004). Most existing CFPD models have assumed the lung airways are rigid (Y Feng & C Kleinstreuer, 2013; Yu Feng & Clement Kleinstreuer, 2013; Feng & Kleinstreuer, 2014; Feng et al., 2015; Xi et al., 2016; Feng, Zhao, Chen, & Lin, 2017; Tian et al., 2016), which limited their realism of modeling lung compliance, and the accuracy of the prediction of local and regional drug deposition data from mouth/nose to G23 with alveoli. It is necessary to model the deformation of lung airways to achieve more realistic internal airflow and pressure distributions, and the accurate predictions of the resultant PM and vapor fates. Research efforts have been done to develop an elastic lung model to simulate airflow and aerosol dynamics in certain pulmonary regions (Aghasafari & Pidaparti, 2018; Heravi, Nazari, Chouly, Perrier, & Payan, 2016; Hofemeier & Sznitman, 2016; Kolanjiyil & Kleinstreuer, 2017; Malvè et al., 2011; Seyfi, Santhanam, & Ilegbusi, 2016; Seyfi Noferest, Santhanam, & Ilegbusi, 2018; Subramaniam et al., 2017; Sul et al., 2019; Talaat & Xi, 2017; Wall & Rabczuk, 2008; Wall, Wiechert, Comerford, & Rausch, 2010; J. Wang et al., 2019; Werner, Ehrhardt, Schmidt, & Handels, 2008; Xi, Talaat, & Si, 2018; Xi, Wang, et al., 2018; Xia, Tawhai, Hoffman, & Lin, 2010; Zhao et al., 2020), i.e., lung lobe movement, alveolar movement, bronchioles movement, trachea-to-bronchi movement, uvula motion, and glottis motion. The numerical approaches used include dynamic mesh, one-way FSI, and two-way FSI. Considering the computational efficiency, it is preferred to employ a dynamic mesh method with sufficient support from 4D CT images to accurately define the localized airway displacements. Two in-house research efforts using the dynamic mesh method are presented here with detailed governing equations.

4.2.1.1. Moving glottis model. The glottis abduction and adduction motion can significantly influence the airflow field in the upper airway (Scheinherr et al., 2012, 2015). Based on the dynamic mesh method, a generalized glottis motion function (Zhao et al., 2020) has been developed validated with clinical data (Scheinherr et al., 2012, 2015) to capture the transient aperture variations of the glottis. Specifically, the in-house glottal motion function that determines the displacement $y(x,t)$ of each node in the dynamic glottis region was modeled using the product of a temporal Fourier series $g(t)$ and a spatial sinusoidal function $f(x)$, i.e.,

$$y(x,t) = \left(d_{g,r} - 1\right) f(x) g(t) + y_{r,0} \tag{34}$$

$$g(t) = a_0 + \sum_{\beta=1}^{n} [a_\beta \cos(\beta\omega t) + b_\beta \sin(\beta\omega t)] \tag{35}$$

$$f(x) = \sin^m\left(\frac{x(t) - x_1}{x_2 - x_1}\pi\right) \tag{36}$$

where $y_{r,0}$ is the initial y-coordinate of the node, and $d_{g,r}$ is the ratio between maximum glottis width and the width of the glottis at the neutral position (t = 0 s). The nodal displacement function $g(t)$ is a time-dependent Fourier series that controls the subject-specific nodal motion separately. a_i and b_i are coefficients that can be calibrated with subject-specific clinical data to control the temporal glottis motion. In Eq. (33), $f(x)$ controls the motion of the glottis region along the x-direction (i.e., the centerline direction of the airway) to achieve a smooth transition from the maximum vocal fold deformation to the zero-displacement airways. Index m can also be calibrated with clinical data to describe subject-specific glottis motion by controlling non-uniform spatial nodal displacement. More details can be found in Zhao et al. (Zhao et al., 2020).

4.2.1.2. Deformable lung airway model (DLAM). A prototype of the deformable lung airway model (DLAM) was developed to dynamically simulate heterogeneous lung inflation and deflation by incorporating a dynamic mesh method to capture lung airway deformations. By integrating the airway moving velocity u_i^m, the Navier-Stokes equation (see Eq. (2)) can be updated as:

$$\frac{\partial u_i}{\partial t} + \left(u_j - u_j^m\right)\frac{\partial u_i}{\partial x_j} = -\frac{1}{\rho_f}\frac{\partial p}{\partial x_i} + \frac{1}{\rho_f}\frac{\partial \tau_{ij}}{\partial x_j} + g_i \tag{37}$$

Here, u_i^m is the dynamic mesh velocity vector. Because of the deformable airway motions, the convective velocity $u_i - u_i^m$ in Eq. (37) is induced by the difference between the localized air velocity and the dynamic mesh velocity. u_i^m is defined by the temporal derivative of coordinates x_i^m of mesh nodes on airway surfaces, i.e.,

$$u_i^m = \frac{\partial x_i^m}{\partial t} \tag{38}$$

Specifically, with the non-slip boundary conditions at airway walls, airflow velocity on moving airway boundaries $u_i|_w$ can be expressed as:

$$u_j|_w = u_j^m|_w \tag{39}$$

The lung airway motion is achieved by simulating the anisotropic expansion and compression with realistic volume changes based on pulmonary function test (PFT) statistics (Bates, & T., 2009; West, 1979). One-way coupled fluid-structure interactions (FSIs) between lung motion and airflow is employed. In fact, the air has a low density and the induced stress tensor effect on lung deformation is negligible, compared with the diaphragm movement, which drives lung motion. Because lower airway configurations are missing in the subject-specific airway geometries, the lower airway volume change induced airflow is not able to be modeled explicitly. To address this issue and make the dynamic mesh method compatible with the geometries without lower airways, DLAM integrated an innovative 2-stage methodology to describe the airway deformation dynamics with realistic whole-lung volume changes over time.

4.2.1.2.1. Upper airway deformation. For upper airway geometry in Fig. 14, deformations are achieved using dynamic mesh. The deformation is governed by an in-house user-defined function (UDF), which calculates the nodal coordinates of airway walls and the adjacent flow domain at each time step. Specifically, at time t, the coordinate x_i (i = 1,2,3) of any point of the lung (or lung airways)

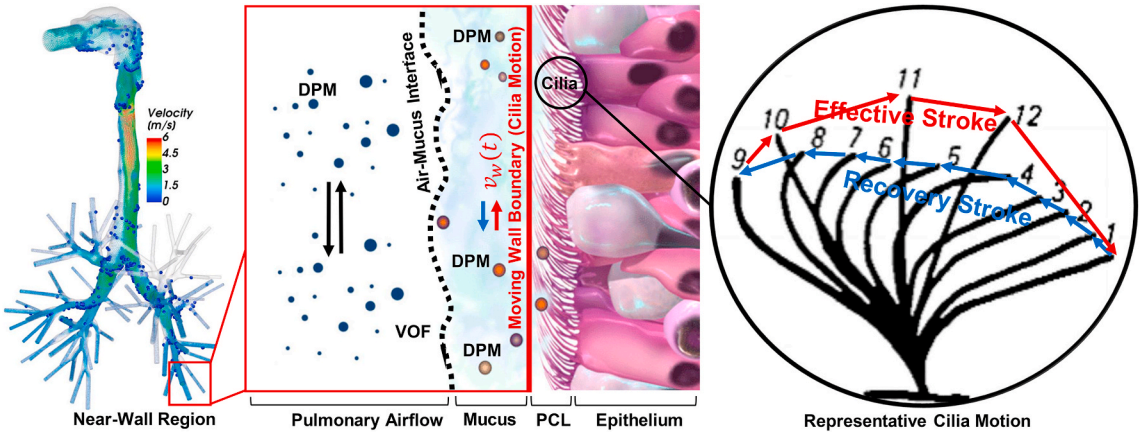

Fig. 15. The VOF-DPM modeling framework for the air-mucus-particle transport with the moving boundary conditions mimicking the transient cilia beating velocity.

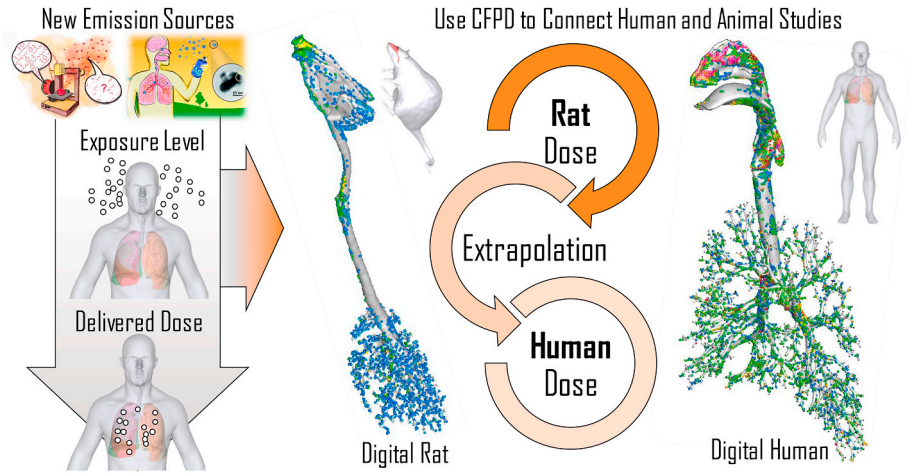

Fig. 16. The schematic of a precise scale-up method to predict lung delivered dose in human using animal data.

can be calculated by:

$$x_i^m(t) = \left(x_i^m(0) - x_{i,ref}^m\right) \cdot B_i(t) \tag{40}$$

where $x_i^m(0)$ is the initial coordinates of nodes at the start of inhalation, and $x_{i,ref}^m$ is the coordinates of the stationary reference point, i.e., the geometric center of the reference cross-section (see Fig. 14). The transforming function vector $B_i(t)$ can be given as:

$$B_i(t) = 1 + 0.5b_i - 0.5b_i\cos(2\pi f \cdot t) \tag{41}$$

where f [Hz] is the frequency, i.e., the number of breath cycles per second. b_i is the deformation ratio vector (see Fig. 14 for the definition), of which the value changes with directions and breathing patterns. Specifically, the anisotropic deformation ratio along the three directions is given by (Bates & T., 2009; De Groote et al., 1997; Plathow et al., 2004; West, 1979; Xi, Talaat, et al., 2018) :

$$b_x : b_y : b_z = 1 : 0.375 : 1 \tag{42}$$

where the restricted deformation ratio along left-to-right y-direction is limited by the rib cage. b_i varies with different breathing intensities, which can be categorized by the total inspiratory volume (TIV) expressed as a multiple of the tidal volume (TV), i.e., $\beta \cdot TV$. TIV is defined as the volume of air taken into the lungs with each inspiration. Based on the physiologic data from measurements of lung mechanical functions (De Groote et al., 1997; Plathow et al., 2004; West, 1979; Xi, Talaat, et al., 2018), the ratio between tidal volume (TV) and functional residual capacity (FRC) for healthy subjects can be assumed as 7:30.

4.2.1.2.2. Inspiratory and expiratory flow rate for lower airway deformation compensation. In the DLAM model, the ventilation was generated by the positive or negative pressure relative to atmospheric due to the realistic elastic lung volume changes. Due to the unavailability of generating peripheral airway configurations, the portion of respiratory flow rate due to the lower airway deformation cannot be considered using the same modeling strategy. Therefore, a compensational volumetric flow rate $Q_{LA,k}$ is applied and distributed at each truncated airway end of the reconstructed respiratory system (see Fig. 14), to match the realistic TIV based on PFT data. Assuming the total computational volumetric flow rate $\sum_k Q_{LA,k}$ can be expressed as:

$$\sum_k Q_{LA,k} = PIFR_{LA} \cdot \sin(2\pi f \cdot t) \tag{43}$$

where $PIFR_{LA}$ is the compensational peak inspiratory flow rate, which should satisfy:

$$TIV_{LA} = \int_0^{\frac{1}{2f}} PIFR_{LA} \cdot \sin(2\pi f \cdot t)dt = \frac{(FRC_{WL} - FRC_{UA})\beta \cdot TV_{WL}}{FRC_{WL}} \tag{44}$$

Therefore,

$$PIFR_{LA} = \frac{\pi f(FRC_{WL} - FRC_{UA})\beta \cdot TV_{WL}}{FRC_{WL}} \tag{45}$$

4.2.2. Whole-lung models

High-resolution lung deposition data are crucial in the precise occupational exposure risk assessment. Because of the small sizes, small particles, including $PM_{2.5}$ and toxic gases, are respirable and can penetrate the peripheral lung and enter the systemic region via

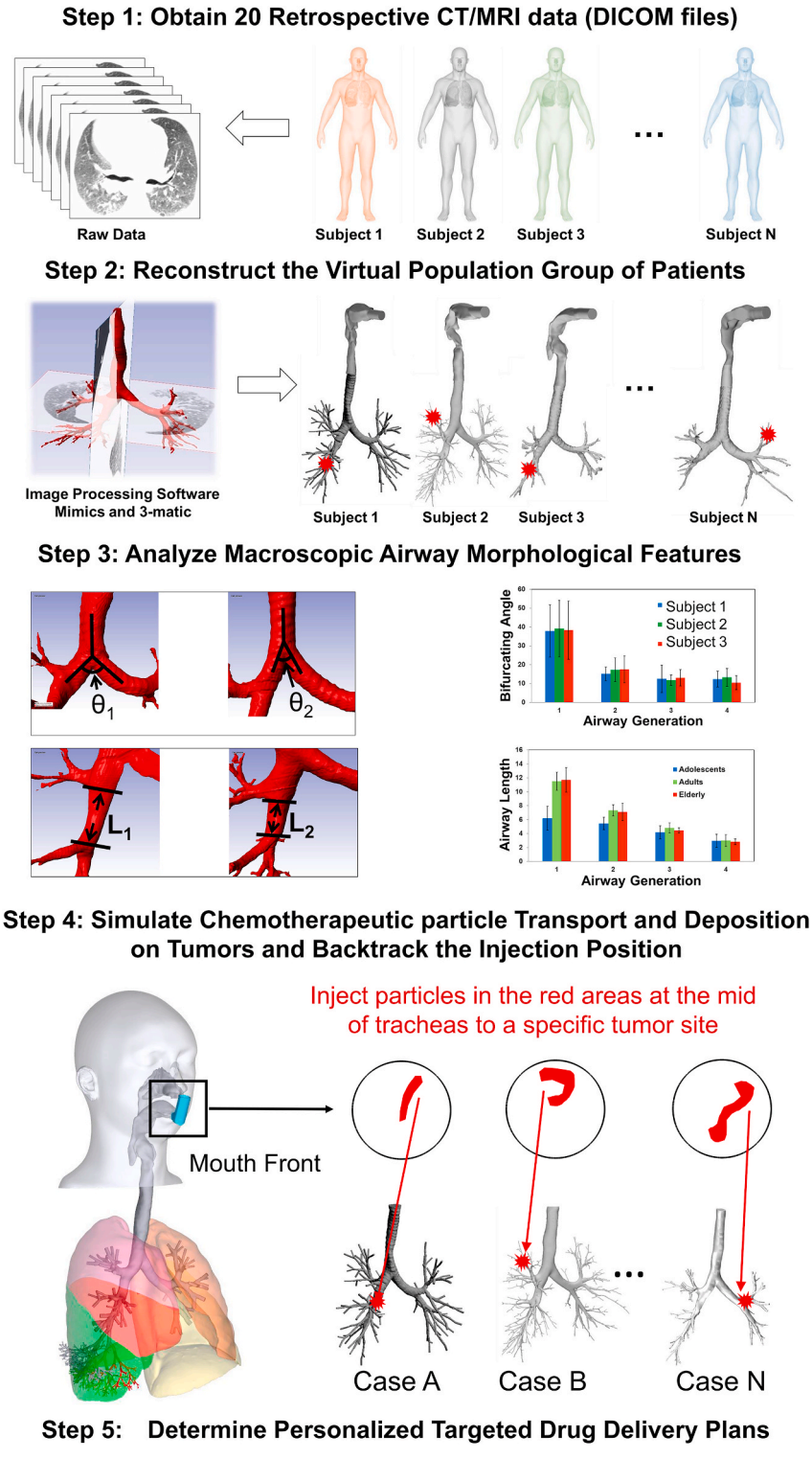

Fig. 17. The investigation framework of the inter-subject variability effect on lung aerosol dynamics using CFPD models for personalized treatment plan optimization for targeted chemotherapeutic drug delivery to treat lung cancer.

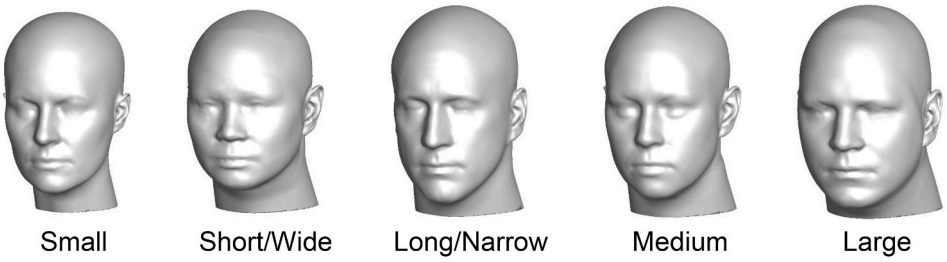

Fig. 18. Representative human head forms based on the anthropometric database built by NIOSH (Zhuang and Bradtmiller, 2005).

the air-blood barriers (Choi & Kim, 2007; Comerford, Forster, & Wall, 2010; Dong, Shang, Inthavong, Chan, & Tu, 2018; Haghnegahdar et al., 2018; Inthavong, Tian, Tu, Yang, & Xue, 2008; Kolanjiyil & Kleinstreuer, 2013; AKolanjiyil & Kleinstreuer, 2013; A. V. Kolanjiyil & C Kleinstreuer, 2016; Arun V Kolanjiyil & Kleinstreuer, 2017; Kolanjiyil, Kleinstreuer, & Sadikot, 2017; Koullapis, Nicolaou, & Kassinos, 2018; Longest et al., 2012; Longest, Tian, Khajeh-Hosseini-Dalasm, & Hindle, 2016; Tawhai, Pullan, & Hunter, 2000; Tena, Fernandez, Alvarez, Casan, & Walters, 2016; Walters & Luke, 2011;Zhang, Kleinstreuer, & Kim, 2008). Accordingly, to predict the translocation of those toxic species after their deposition using PBPK/TK models, local and regional drug deposition data in the whole respiratory systems from mouth/nose to alveoli must be provided as precise inputs. Therefore, whole-lung modeling capabilities are not only able to provide a full map of regional depositions of inhaled PM and gases, but also enable the accurate simulation of expiratory particle and gas dynamics after the inhalation. Most existing simulations use the truncated subject-specific airway geometries reconstructed from CT/MRI data only contain airways up to generation 9 (G9) . The missing lower airways force the researchers to make assumptions on how many inhaled particles will be able to "re-enter" the flow domain back from the truncated airway terminals during the exhalation. With the whole-lung modeling strategies, the lung PM dynamics during the full inhalation-exhalation cycles can be predicted without such ad-hoc simplifications. Thus, it is necessary to simulate drug particle transport and deposition in a domain covering the entire conducting and respiratory zones. Research efforts have been made for whole-lung model developments with modeling strategies employed as follows:

(1) Using trumpet geometry to represent the whole tracheobronchial tree (Cui, Wu, & Ge, 2020; Hasler et al., 2019; Arun V Kolanjiyil & Clement Kleinstreuer, 2016),
(2) Reducing the degree of freedom (DOF) the whole lung airway trees by truncating airways and applying advanced coupled boundary conditions, to generate single-path and multiple-path whole-lung models (A. V. Kolanjiyil & C. Kleinstreuer, 2013; A. V. Kolanjiyil & C Kleinstreuer, 2016; Pandal-Blanco, Barrio-Perotti, Agujetas-Ortiz, & Fernandez-Tena, 2019; Tawhai et al., 2000; Tena et al., 2016; Walters & Luke, 2011; Wu, Miyawaki, Tawhai, Hoffman, & Lin, 2015), and
(3) Simplifying small airways using 1D pipelines or 2D in-plane airway models instead of 3D geometries (Tawhai et al., 2000; Zhang et al., 2008).

Currently, the idea to reconstruct a full 3D subject-specific whole-lung model is still not feasible due to difficulties in small-airway segmentation using CT/MRI images. Even if the entire lung was fully segmentable, it is not computationally feasible to simulate the full lung tree accurately, since it requires billions of mesh elements (Comerford et al., 2010; A. V. Kolanjiyil & C Kleinstreuer, 2016; Pandal-Blanco et al., 2019), and the computational time is not affordable. However, with the increase in computational power, the long-term goal of the virtual lung model should still be the creation of subject-specific lung containing the entire 3D respiratory and conductive zones.

4.2.3. Cilia-driven mucus movement models

The fate of deposited particles in the lung is a complex function of the kinetics of absorption and non-absorptive clearance mechanisms (Silberberg, 1982; Spagnolie, 2015). Mucociliary clearance and interaction with the airflow are two main mechanisms to remove the mucus away from pulmonary airways (Fahy & Dickey, 2010; Levy, Hill, Forest, & Grotberg, 2014; van der Schans, Postma, Koeter, & Rubin, 1999). In reality, the deposited particles will first contact and submerse into the mucus layer within the airways, or the surfactant-lining fluid layer within the alveolar region. Insoluble and non-reactive nanoparticles and most micron particles are not able to be rapidly absorbed and will undergo mucus clearance or physical translocation associated with epithelial cells and cells of the host-defense system for particle-cell interaction. Hence, modeling of lung clearance mechanism is significant for understanding the fate of inhaled PM and gases. Although *in vitro* experiments have been done with simplifications to investigate the mechanism of mucus clearance driven by airflow (Camassa, Forest, Lee, Ogrosky, & Olander, 2012; C. S. Kim, M. A. Greene, S. Sankaran, & M. A. Sackner, 1986; Kim, Iglesias, & Sackner, 1987; Kim, Rodriguez, Eldridge, & Sackner, 1986; King, Brock, & Lundell, 1985), it still lacks *in vivo* studies to investigate the behaviors of the mucus clearance process. The CFD method has also been employed to investigate the mucus movement in the pulmonary system (Paz, Suarez, Vence, & Cabarcos, 2019; Rajendran & Banerjee, 2019). Specifically, Paz et al. (2019) employed a transient Volume of Fluid (VOF) model to study the mucus clearance from mouth to trachea and discovered that an oscillating airflow can enhance the clearance by up to 5% than a steady-state airflow. Rajendran et al. (2019) employed a VOF model to study mucus transport and distribution with steady-state expiration in an idealized airway geometry. Existing CFD efforts (Paz et al., 2019; Rajendran & Banerjee, 2019) are not able to explicitly or realistically simulate the cilia motion and the driven mucus transport

phenomena, due to the computational efficiency problem. Indeed, the discrete element method (DEM), the overset mesh can be employed to explicitly simulate the motion of individual cilium, and the resulting ambient mucus flow. However, such methods are not realistic to be combined with the CFPD modeling framework, since they are computationally expensive. A feasible way is to build a VOF plus Discrete Phase Model (VOF-DPM) with moving boundary conditions, to explicitly model how cilia beats drive the mucus, and track the air-mucus mixture, and trace the mucus clearance effect (see Fig. 15 for the modeling framework). The moving wall boundary conditions, i.e., the transient cilia beating velocities will be applied. Specifically, following the physiologically realistic beating patterns (Gueron & Levit-Gurevich, 1998; Smith, Gaffney, & Blake, 2008), the wall velocity will be given in the form of a Fourier series (Fulford & Blake, 1986). The cilia lengths are from 5 to 8 μm, the diameters are from 0.15 to 0.3 μm and cilia spacings are from 20 to 40 μm ((Spagnolie, 2015)). Frequency of beat, duration of rest, and other clinical measurements to set up the numerical model will also be acquired from open literature (Spagnolie, 2015). The cilia beating velocity can be assigned at each center of the wall face cell.

4.2.4. *Inter-species variability studies*

As surrogates to human beings, rats and other animals are used in experiments to study the exposure risks by inhaling airborne toxicants. To speculate human responses from animal studies, scale-up factors are widely used to extrapolate lung delivered doses from animal to human. However, available scale-up methods are highly simplified and not accurate, because they directly use the human-to-rat ratios of body weights (RBW) or lung surface areas (RSA) as the scale-up factors. However, current scale-up methods between mouse and human are highly simplified and inaccurate, which will result in misleading speculations of animal data to a human, because they all neglected the distinct pulmonary system anatomical differences among different species (see Fig. 16). Thus, it is necessary to develop a scale-up method to precisely characterize the inter-species differences. For precise inter-species scale-up correlations considering lung morphology and breathing pattern differences, it is necessary to obtain local deposition patterns in both animals and humans. Efforts have been made using CFPD-PBPK/TK model to investigate the inter-species variabilities inter-species variabilities on pharmacokinetic and toxicokinetic differences in pulmonary routes for vapor and solid particle transport dynamics (Corley et al., 2012, 2015). Based on the high-resolution lung deposition data and PK/TK data, more physiologically accurate inter-species extrapolations can be precisely done. The schematic is shown in Fig. 16. The potential challenge is the difficulties in reconstructing animal airway geometries, because of the relatively small dimensions of their airways compared to humans.

4.2.5. *Inter-subject variability studies*

4.2.5.1. Inter-subject variabilities in human respiratory systems. Numerical results (Feng, Zhao, et al., 2018; Feng, Chen, & Zhao, 2018; Feng, Zhao, Chen, & Lin, 2017) indicate that the effect of inter-subject variability of human respiratory systems on inhaled particle transport and deposition can be significant. Most computational lung aerosol dynamic studies rely on the numerical results only in one lung airway configuration. They have not yet incorporated subject variability in airflow distributions and aerosol depositions. Therefore, it is inevitable to improve the statistical robustness of the *in silico* study process for lung aerosol dynamics, by using multiple subject-specific human respiratory system geometries, i.e., the virtual human population group (VPG). The development of such VPGs will open up the possibility to comprehensively analyze variations in the general population or for specific subpopulations, resulting in the enhancement of the statistical robustness of the CFPD-PBPK/TK studies. Using the personalized targeted drug delivery planning as an example, the VPG idea is shown in Fig. 17. Open CT/MRI scanned data libraries can be utilized to build the virtual population groups and address the effect of inter-subject variabilities in airway morphologies (COPDGene, 2019; NBIA, 2019; Scans, 2020).

4.2.5.2. Inter-subject variabilities of human body shells. In existing CFPD studies for occupational exposure risk assessments (Chen & Zhao, 2010; Gupta, Lin, & Chen, 2011; He, Niu, Gao, Zhu, & Wu, 2011; Li, Shang, Yan, Yang, & Tu, 2018; Yang, Kang, Hwang, & Park, 2017; Zhang & Li, 2012; Zhao et al., 2019; Zhu, Kato, & Yang, 2006), virtual human body shells have been reconstructed using different anthropometric dimensions. All reconstruction efforts neglected the inter-subject variabilities of the body shell, especially the head and face features, which may influence the PM fate around the head region and the subsequent deposition in the pulmonary respiratory system.

Such inter-subject variability issue in numerical studies have been identified, and ongoing research efforts have been initiated accordingly. For example, the National Institute for Occupational Safety and Health (NIOSH) conducted a nationwide anthropometric survey of 3997 subjects (Zhuang & Bradtmiller, 2005). The resulting head and face measurements were used to develop an anthropometric database detailing the face size distributions of respirator users by both traditional measurement methods and three-dimensional (3D) scanning systems. From the 3997-subject anthropometric survey, 1013 subjects were scanned. As shown in Fig. 18, 3D scans of five individuals, who most closely represented a given size category, were averaged to construct a representative head form for each category (small, medium, large, long/narrow, and short/wide). The NIOSH digital head forms are symmetric and can represent the facial size and shape distribution of current U.S. respirator users. NIOSH encourages the application of the data and results to address occupational safety and health issues.

5. Summary

This paper outlined the fundamental principles and detailed modeling procedures for the CFPD-PBPK/TK method, to simulate the transport, deposition, and translocation of particulate matter (PM) and vapors/gases in human respiratory systems. The paper aims to reduce the confusion among readers who are interested in learning the modeling framework, with emphasis on the key steps to

guarantee the reliability of the numerical simulations. The paper also highlights the difficulties and deficiencies of the current CFPD-PBPK/TK models, and manifests the promising research directions, paving the way to build the next-generation virtual lung-modeling framework. The long-term goal is to develop a personalized physiologically realistic virtual human system and virtual environments based on the CFPD-PBPK/TK modeling framework, to achieve noninvasive precise health risk assessments, by simulating the full process of generation, dispersion, inhalation, pulmonary transport, and systemic region translocations of airborne PM and vapors/gases. Complementing experiments, the CFPD-PBPK/TK model will be beneficial to unveil the underlying aerosol dynamics non-invasively, and significantly reduce the research cycles on addressing occupational safety and health issues.

About this article

This article is an Editor-Invited Tutorial Article. Tutorial articles, established to commemorate the 50th Anniversary of the Journal of Aerosol Science in 2020, are intended to serve as educational resources for the aerosol research community on state-of-the-art experimental, theoretical, and numerical techniques in aerosol science.

Declaration of competing interest

The authors declare that they have no known competing financial interests or personal relationships that could have appeared to influence the work reported in this paper.

Acknowledgment

The use of ANSYS software (Canonsburg, PA) as part of the ANSYS-OSU academic partnership agreement is gratefully acknowledged (Dr. Thierry Marchal, Global Industry Director). The research was partially funded through the award for project number HR19-106, from the Oklahoma Center for the Advancement of Science and Technology (OCAST).

References

Aghasafari, P., & Pidaparti, R. (2018). Influence of tidal-volume setting, emphysema and ARDS on human alveolar sacs mechanics. *Acta Mechanica Sinica, 34*(5), 983–993.

Ahmed, S. A., & Giddens, D. P. (1983a). Flow disturbance measurements through a constricted tube at moderate Reynolds numbers. *Journal of Biomechanics, 16*(12), 955–963.

Ahmed, S. A., & Giddens, D. P. (1983b). Velocity measurements in steady flow through axisymmetric stenoses at moderate Reynolds numbers. *Journal of Biomechanics, 16*(7), 505–516.

Alzahrany, M., Banerjee, A., & Salzman, G. (2014). The role of coupled resistance–compliance in upper tracheobronchial airways under high frequency oscillatory ventilation. *Medical Engineering & Physics, 36*(12), 1593–1604.

Alzahrany, M. S. (2014). *Pulmonary gas transport and drug delivery in a patient specific lung model during invasive high frequency oscillatory ventilation. (Doctor of Philosophy)* (p. 1414). Lehigh University.

Asgari, M., Lucci, F., & Kuczaj, A. K. (2019). Multispecies aerosol evolution and deposition in a bent pipe. *Journal of Aerosol Science, 129*, 53–70.

Asgharian, B., Hofmann, W., & Miller, F. (2001). Mucociliary clearance of insoluble particles from the tracheobronchial airways of the human lung. *Journal of Aerosol Science, 32*(6), 817–832.

ASME V&V 40 Subcommittee on Verification and Validation of Computational Modeling for Medical Devices. (2018). *Assessing Credibility of Computational Modeling through Verification and Validation: Application to Medical Devices* (pp. 1–60). ASME.

Bakand, S., & Hayes, A. (2016). Toxicological considerations, toxicity assessment, and risk management of inhaled nanoparticles. *International Journal of Molecular Sciences, 17*(6), 929.

Banko, A., Coletti, F., Schiavazzi, D., Elkins, C., & Eaton, J. (2015). Three-dimensional inspiratory flow in the upper and central human airways. *Experiments in Fluids, 56*(6), 117.

Bates, J. H. T. (2009). *Lung mechanics (an inverse modeling approach) || the general linear model*.

Ben-Nasr, O., Hadjadj, A., Chaudhuri, A., & Shadloo, M. S. (2017). Assessment of subgrid-scale modeling for large-eddy simulation of a spatially-evolving compressible turbulent boundary layer. *Computers & Fluids, 151*, 144–158.

Bernate, J. A., Geisler, T. S., Padhy, S., Shaqfeh, E. S., & Iaccarino, G. (2017). Study of the flow unsteadiness in the human airway using large eddy simulation. *Physical Review Fluids, 2*(8), 083101.

Bobbio, A., Chetta, A., Carbognani, P., Internullo, E., Verduri, A., Sansebastiano, G., … Olivieri, D. (2005). Changes in pulmonary function test and cardio-pulmonary exercise capacity in COPD patients after lobar pulmonary resection. *European Journal of Cardio-Thoracic Surgery, 28*(5), 754–758.

Bui, V. K. H., Moon, J.-Y., Chae, M., Park, D., & Lee, Y.-C. (2020). Prediction of aerosol deposition in the human respiratory tract via computational models: A review with recent updates. *Atmosphere, 11*(2), 137.

Cui, X., Wu, W., & Gutheil, E. (2018). Numerical study of the airflow structures in an idealized mouth-throat under light and heavy breathing intensities using large eddy simulation. *Respiratory Physiology & Neurobiology, 248*, 1–9.

de Camargo, A. A., Justino, T., de Andrade, C. H. S., Malaguti, C., & Dal Corso, S. (2011). Chester step test in patients with COPD: Reliability and correlation with pulmonary function test results. *Respiratory Care, 56*(7), 995–1001.

Camassa, R., Forest, M. G., Lee, L., Ogrosky, H. R., & Olander, J. (2012). Ring waves as a mass transport mechanism in air-driven core-annular flows. ARTN 066305 *Physical Review E, 86*(6), 10.1103/PhysRevE.86.066305.

Chen, X., Feng, Y., Zhong, W., & Kleinstreuer, C. (2017). Numerical investigation of the interaction, transport and deposition of multicomponent droplets in a simple mouth-throat model. *Journal of Aerosol Science, 105*, 108–127.

Cheng, K.-H., Cheng, Y.-S., Yeh, H.-C., Guilmette, R. A., Simpson, S. Q., Yang, Y.-H., et al. (1996). In vivo measurements of nasal airway dimensions and ultrafine aerosol deposition in the human nasal and oral airways. *Journal of Aerosol Science, 27*(5), 785–801.

Chen, X., Kleinstreuer, C., Zhong, W., Feng, Y., & Zhou, X. (2018). Effects of thermal airflow and mucus-layer interaction on hygroscopic droplet deposition in a simple mouth–throat model. *Aerosol Science and Technology, 52*(8), 900–912.

Chen, C., & Zhao, B. (2010). Some questions on dispersion of human exhaled droplets in ventilation room: Answers from numerical investigation. *Indoor Air, 20*(2), 95–111.

Chen, X., Zhou, X., Xia, X., Xie, X., Lu, P., & Feng, Y. (2020). Modeling of the transport, hygroscopic growth, and deposition of multi-component droplets in a simplified airway with realistic thermal boundary conditions. *Journal of Aerosol Science*, 105626.

Choi, J. I., & Kim, C. S. (2007). Mathematical analysis of particle deposition in human lungs: An improved single path transport model. *Inhalation Toxicology, 19*, 925–939.
Choi, J., Tawhai, M. H., Hoffman, E. A., & Lin, C.-L. (2009). On intra- and intersubject variabilities of airflow in the human lungs. *Physics of Fluids, 21*(10), 101901. https://doi.org/10.1063/1.3247170
Chuang, H.-C. (2019). *Oxidative stress in environmental lung diseases oxidative Stress in lung diseases* (pp. 293–307). Springer.
Collier, G., Wild, J., Oates, G., & Chung, Y. (2013). Velocity mapping of gasflow in the upper airways of a lung model for validation of computational fluid dynamics simulations. In *Paper presented at the proceedings of the 21st annual meeting of ISMRM, salt lake city, Utah, USA*.
Comerford, A., Forster, C., & Wall, W. A. (2010). Structured tree impedence outflow boundary conditions for 3D lung simulations. *Journal of Biomechanical Engineering, 132*, 10.
COPDGene. (2019). COPDGene. Retrieved from http://www.copdgene.org/.
Corley, R. A., Kabilan, S., Kuprat, A. P., Carson, J. P., Jacob, R. E., Minard, K. R., … Glenny, R. (2015). Comparative risks of aldehyde constituents in cigarette smoke using transient computational fluid dynamics/physiologically based pharmacokinetic models of the rat and human respiratory tracts. *Toxicological Sciences, 146*(1), 65–88.
Corley, R. A., Kabilan, S., Kuprat, A. P., Carson, J. P., Minard, K. R., Jacob, R. E., … Cox, T. (2012). Comparative computational modeling of airflows and vapor dosimetry in the respiratory tracts of rat, monkey, and human. *Toxicological Sciences, 128*(2), 500–516.
Cui, X., & Gutheil, E. (2011). Large eddy simulation of the unsteady flow-field in an idealized human mouth–throat configuration. *Journal of Biomechanics, 44*(16), 2768–2774.
Cui, X., & Gutheil, E. (2018). Large eddy simulation of the flow pattern in an idealized mouth-throat under unsteady inspiration flow conditions. *Respiratory Physiology & Neurobiology, 252–253*, 38–46.
Cui, X., Wu, W., & Ge, H. (2020). Investigation of airflow field in the upper airway under unsteady respiration pattern using large eddy simulation method. *Respiratory Physiology & Neurobiology*, 103468.
De Groote, A., Wantier, M., Chéron, G., Estenne, M., & Paiva, M. (1997). Chest wall motion during tidal breathing. *Journal of Applied Physiology, 83*(5), 1531–1537.
Dong, J., Ma, J., Shang, Y., Inthavong, K., Qiu, D., Tu, J., et al. (2018). Detailed nanoparticle exposure analysis among human nasal cavities with distinct vestibule phenotypes. *Journal of Aerosol Science, 121*, 54–65.
Einstein, A. (1908). Elementare theorie der brownschen) bewegung. *Zeitschrift für Elektrochemie und angewandte physikalische Chemie, 14*(17), 235–239.
Fahy, J. V., & Dickey, B. F. (2010). Airway mucus function and dysfunction. *New England Journal of Medicine, 363*(23), 2233–2247.
Fan, L., Xia, Y., Guan, Y., Zhang, T.f., & Liu, S.y. (2014). Characteristic features of pulmonary function test, CT volume analysis and MR perfusion imaging in COPD patients with different HRCT phenotypes. *The clinical respiratory journal, 8*(1), 45–54.
Farghadan, A., Poorbahrami, K., Jalal, S., Oakes, J. M., Coletti, F., & Arzani, A. (2020). Particle transport and deposition correlation with near-wall flow characteristic under inspiratory airflow in lung airways. *Computers in Biology and Medicine, 120*, Article 103703.
Feng, Y., Chen, X., & Zhao, J. (2018). Create the individualized digital twin for noninvasive precise pulmonary healthcare. *Significances of Bioengineering & Biosciences, 1*(2), 26–30.
Feng, Y., & Kleinstreuer, C. (2013a). Analysis of non-spherical particle transport in complex internal shear flows. *Physics of Fluids, 25*(9), 091904.
Feng, Y., & Kleinstreuer, C. (2013b). DDPM-DEM simulations of particulate flows in human tracheobronchial airways. In *Paper presented at the ASME 2013 international mechanical engineering congress and exposition*.
Feng, Y., & Kleinstreuer, C. (2014). Micron-particle transport, interactions and deposition in triple lung-airway bifurcations using a novel modeling approach. *Journal of Aerosol Science, 71*, 1–15.
Feng, Y., Kleinstreuer, C., Castro, N., & Rostami, A. (2016). Computational transport, phase change and deposition analysis of inhaled multicomponent droplet–vapor mixtures in an idealized human upper lung model. *Journal of Aerosol Science, 96*(6), 96–123.
Feng, Y., Kleinstreuer, C., & Rostami, A. (2015). Evaporation and condensation of multicomponent electronic cigarette droplets and conventional cigarette smoke particles in an idealized G3–G6 triple bifurcating unit. *Journal of Aerosol Science, 80*, 58–74.
Feng, Y., Marchal, T., Sperry, T., & Yi, H. (2020). Influence of wind and relative humidity on the social distancing effectiveness to prevent COVID-19 airborne transmission: A numerical study. *Journal of Aerosol Science, 147*, 105585.
Feng, Y., Xu, Z., & Haghnegahdar, A. (2016). *Computational fluid-particle dynamics modeling for unconventional inhaled aerosols in human respiratory systems aerosols-Science and case studies* (pp. 49–84). InTech.
Feng, Y., Zhao, J., Chen, X., & Lin, J. (2017). An in silico subject-variability study of upper airway morphological influence on the airflow regime in a tracheobronchial tree. *Bioengineering, 4*(4), Article 90.
Feng, Y., Zhao, J., Kleinstreuer, C., Wang, Q., Wang, J., Wu, D. H., et al. (2018). An in silico inter-subject variability study of extra-thoracic morphology effects on inhaled particle transport and deposition. *Journal of Aerosol Science, 123*, 185–207.
Ferron, G. A., Oberdorster, G., & Henneberg, R. (1989). Estimation of the deposition of aerosolized drugs in the human respiratory tract due to hygroscopic growth. *Journal of Aerosol Medicine, 2*(3), 271–284.
Ferron, G. A., Upadhyay, S., Zimmermann, R., & Karg, E. (2013). Model of the deposition of aerosol particles in the respiratory tract of the rat. II. Hygroscopic particle deposition. *Journal of Aerosol Medicine and Pulmonary Drug Delivery, 26*, 101–118.
Ferziger, J. H., & Perić, M. (1996). Further discussion of numerical errors in CFD. *International Journal for Numerical Methods in Fluids, 23*(12), 1263–1274.
Frederick, C. B., Lomax, L. G., Black, K. A., Finch, L., Scribner, H. E., Kimbell, J. S., … Morris, J. B. (2002). Use of a hybrid computational fluid dynamics and physiologically based inhalation model for interspecies dosimetry comparisons of ester vapors. *Toxicology and Applied Pharmacology, 183*(1), 23–40.
Frederix, E., Kuczaj, A. K., Nordlund, M., Bělka, M., Lizal, F., Jedelský, J., … Geurts, B. (2018). Simulation of size-dependent aerosol deposition in a realistic model of the upper human airways. *Journal of Aerosol Science, 115*, 29–45.
Fulford, G. R., & Blake, J. R. (1986). Muco-ciliary transport in the lung. *Journal of Theoretical Biology, 121*(4), 381–402.
Garimella, R. V., Kim, J., & Berndt, M. (2014). Polyhedral mesh generation and optimization for non-manifold domains. In *Proceedings of the 22nd international meshing roundtable* (pp. 313–330). Springer.
van Geffen, W. H., Hajian, B., Vos, W., De Backer, J., Cahn, A., Usmani, O. S., … De Backer, W. (2018). Functional respiratory imaging: Heterogeneity of acute exacerbations of COPD. *International Journal of Chronic Obstructive Pulmonary Disease, 13*, 1783.
Graham, D. I. (1998). Improved eddy interaction models with random length and time scales. *International Journal of Multiphase Flow, 24*(2), 335–345.
Germano, M., Piomelli, U., Moin, P., & Cabot, W. H. (1991). A dynamic subgrid-scale eddy viscosity model. *Physics of Fluids A: Fluid Dynamics, 3*(7), 1760–1765.
Graham, D., & James, P. (1996). Turbulent dispersion of particles using eddy interaction models. *International Journal of Multiphase Flow, 22*(1), 157–175.
Gueron, S., & Levit-Gurevich, K. (1998). Computation of the internal forces in cilia: Application to ciliary motion, the effects of viscosity, and cilia interactions. *Biophysical Journal, 74*(4), 1658–1676.
Guo, Y., Wei, J., Ou, C., Liu, L., Sadrizadeh, S., Jin, T., & Li, Y. (2020). Deposition of droplets from the trachea or bronchus in the respiratory tract during exhalation: A steady-state numerical investigation. *Aerosol Science and Technology, 54*, 869–879.
Gupta, J. K., Lin, C. H., & Chen, Q. (2011). Transport of expiratory droplets in an aircraft cabin. *Indoor Air, 21*(1), 3–11.
Haghnegahdar, A., Feng, Y., Chen, X., & Lin, J. (2018). Computational analysis of deposition and translocation of inhaled nicotine and acrolein in the human body with e-cigarette puffing topographies. *Aerosol Science and Technology, 52*(5), 483–493.
Haghnegahdar, A., Zhao, J., & Feng, Y. (2019). Lung aerosol dynamics of airborne influenza A virus-laden droplets and the resultant immune system responses: An in silico study. *Journal of Aerosol Science, 134*, 34–55.
Haghnegahdar, A., Zhao, J., Kozak, M., Williamson, P., & Feng, Y. (2019). Development of a hybrid CFD-PBPK model to predict the transport of xenon gas around a human respiratory system to systemic regions. *Heliyon, 5*(4), Article e01461.
Hajian, B., De Backer, J., Vos, W., van Geffen, W. H., De Winter, P., Usmani, O., & De Backer, W. (2018). Changes in ventilation–perfusion during and after an COPD exacerbation: An assessment using fluid dynamic modeling. *International Journal of Chronic Obstructive Pulmonary Disease, 13*, 833–842.

Han, B., Hirahara, H., & Yoshizaki, S. (2016). Streaming caused by oscillatory flow in peripheral airways of human lung. *Open Journal of Fluid Dynamics, 6*(3), 242–261.
Hariprasad, D. S., Sul, B., Liu, C., Kiger, K. T., Altes, T., Ruppert, K., & Wallqvist, A. (2020). Obstructions in the lower airways lead to altered airflow patterns in the central airway. *Respiratory Physiology & Neurobiology, 272*, Article 103311.
Hasler, D., Anagnostopoulou, P., Nyilas, S., Latzin, P., Schittny, J., & Obrist, D. (2019). A multi-scale model of gas transport in the lung to study heterogeneous lung ventilation during the multiple-breath washout test. *PLoS Computational Biology, 15*(6), Article e1007079.
He, Q., Niu, J., Gao, N., Zhu, T., & Wu, J. (2011). CFD study of exhaled droplet transmission between occupants under different ventilation strategies in a typical office room. *Building and Environment, 46*(2), 397–408.
Heravi, F., Nazari, M., Chouly, F., Perrier, P., & Payan, Y. (2016). *Computational fluid dynamics in the upper airway: Comparison between different models and experimental data for a simplified geometry with major obstruction*.
Heyder, J., Gebhart, J., Stahlhofen, W., & Stuck, B. (1982). *Biological variability of particle deposition in the human respiratory tract during controlled and spontaneous mouth-breathing Inhaled Particles V* (pp. 137–147). Elsevier.
Hofemeier, P., & Sznitman, J. (2016). The role of anisotropic expansion for pulmonary acinar aerosol deposition. *Journal of Biomechanics, 49*(14), 3543–3548.
Hofmann, W., Bolt, L., Sturm, R., Fleming, J., & Conway, J. (2005). Simulation of three-dimensional particle deposition patterns in human lungs and comparison with experimental SPECT data. *Aerosol Science and Technology, 39*(8), 771–781.
Hofmann, W., & Sturm, R. (2004). Stochastic model of particle clearance in human bronchial airways. *Journal of Aerosol Medicine, 17*(1), 73–89.
Horsfield, K., & Cumming, G. (1968). Morphology of the bronchial tree in man. *Journal of Applied Physiology, 24*(3), 373–383.
Hu, S., Ben-Jebria, A., & Ultman, J. S. (1994). Longitudinal distribution of ozone absorption in the lung: Effects of respiratory flow. *Journal of Applied Physiology, 77*(2), 574–583.
Inthavong, K. (2020). From indoor exposure to inhaled particle deposition: A multiphase journey of inhaled particles. *Experimental and Computational Multiphase Flow, 2*(2), 59–78.
Inthavong, K., Mouritz, A. P., Dong, J., & Tu, J. Y. (2013). Inhalation and deposition of carbon and glass composite fibre in the respiratory airway. *Journal of Aerosol Science, 65*, 58–68.
Inthavong, K., Tian, Z., Tu, J., Yang, W., & Xue, C. (2008). Optimising nasal spray parameters for efficient drug delivery using computational fluid dynamics. *Computers in Biology and Medicine, 38*(6), 713–726.
Islam, M. S., Saha, S. C., Sauret, E., Gemci, T., & Gu, Y. T. (2017). Pulmonary aerosol transport and deposition analysis in upper 17 generations of the human respiratory tract. *Journal of Aerosol Science, 108*, 29–43.
Islam, M. S., Saha, S. C., Sauret, E., Ong, H., Young, P., & Gu, Y. (2019). Euler–Lagrange approach to investigate respiratory anatomical shape effects on aerosol particle transport and deposition. *Toxicology Research and Application, 3*, 1–15.
Jalal, S., Van de Moortele, T., Amili, O., & Coletti, F. (2020). Steady and oscillatory flow in the human bronchial tree. *Physical Review Fluids, 5*(6), 063101.
Jayaraju, S. T., Brouns, M., Lacor, C., Belkassem, B., & Verbanck, S. (2008). Large eddy and detached eddy simulations of fluid flow and particle deposition in a human mouth–throat. *Journal of Aerosol Science, 39*(10), 862–875.
Jin, H. H., Fan, J. R., Zeng, M. J., & Cen, K. F. (2007). Large eddy simulation of inhaled particle deposition within the human upper respiratory tract. *Journal of Aerosol Science, 38*(3), 257–268.
Johnson, R. W. (2016). *Handbook of fluid dynamics*. Crc Press.
Kadota, K., Inoue, N., Matsunaga, Y., Takemiya, T., Kubo, K., Imano, H., … Tozuka, Y. (2020). Numerical simulations of particle behaviour in a realistic human airway model with varying inhalation patterns. *Journal of Pharmacy and Pharmacology, 72*(1), 17–28.
Kannan, R., Chen, Z. J., Singh, N., Przekwas, A., Delvadia, R., Tian, G., et al. (2017). A quasi-3D wire approach to model pulmonary airflow in human airways. *International Journal for Numerical Methods in Biomedical Engineering, 33*(7), Article e2838.
Katz, I., Murdock, J., Palgen, M., Pype, J., & Caillibotte, G. (2015). Pharmacokinetic analysis of the chronic administration of the inert gases Xe and Ar using a physiological based model. *Medical Gas Research, 5*(1), Article 8.
Kaye, S., & Schroter, R. (1993). *An experimental model of gas dispersion and uptake at the bronchial wall*.
Kelly, J. T., Asgharian, B., Kimbell, J. S., & Wong, B. A. (2004). Particle deposition in human nasal airway replicas manufactured by different methods. Part II: Ultrafine particles. *Aerosol Science and Technology, 38*(11), 1072–1079.
Kenjereš, S., & Tjin, J. L. (2017). Numerical simulations of targeted delivery of magnetic drug aerosols in the human upper and central respiratory system: A validation study. *Royal Society Open Science, 4*(12), 170873.
Keyhani, K., Scherer, P. W., & Mozell, M. M. (1997). A numerical model of nasal odorant transport for the analysis of human olfaction. *Journal of Theoretical Biology, 186*(3), 279–301.
Kim, C. S., Rodriguez, C. R., Eldridge, M. A., & Sackner, M. A. (1986). Criteria for mucus transport in the airways by two-phase gas-liquid flow mechanism. *Journal of Applied Physiology, 60*(3), 901–907.
Kim, S.-E. (2004). Large eddy simulation using an unstructured mesh based finite-volume solver. In *34th AIAA fluid dynamics conference and exhibit: American Institute of aeronautics and astronautics*.
Kim, C. S., & Fisher, D. M. (1999). Deposition characteristics of aerosol particles in sequentially bifurcating airway models. *Aerosol Science & Technology, 31*(2–3), 198–220.
Kim, C. S., Greene, M. A., Sankaran, S., & Sackner, M. A. (1986). Mucus transport in the airways by two-phase gas-liquid flow mechanism: Continuous flow model. *Journal of Applied Physiology, 60*(3), 908–917.
Kim, C. S., Greene, M. A., Sankaran, S., & Sackner, M. A. (1986b). Mucus transport in the airways by two-phase gas-liquid flow mechanism: Continuous flow model. *Journal of Applied Physiology, 60*(3), 908–917.
Kim, C. S., Iglesias, A. J., & Sackner, M. A. (1987). Mucus clearance by two-phase gas-liquid flow mechanism: Asymmetric periodic flow model. *Journal of Applied Physiology, 62*(3), 959–971.
Kim, C. S., & Jaques, P. A. (2004). Analysis of total respiratory deposition of inhaled ultrafine particles in adult subjects at various breathing patterns. *Aerosol Science and Technology, 38*(6), 525–540.
King, M., Brock, G., & Lundell, C. (1985). Clearance of mucus by simulated cough. *Journal of Applied Physiology, 58*(6), 1776–1782.
Klaassen, C. D., & Amdur, M. O. (2013). *Casarett and doull's toxicology: The basic science of poisons, 1236*. New York: McGraw-Hill.
Kleinstreuer, C. (2003). *Two-phase flow: Theory and applications*. CRC Press.
Kleinstreuer, C. (2018). *Modern fluid dynamics*. Springer.
Kleinstreuer, C., & Feng, Y. (2013). Computational analysis of non-spherical particle transport and deposition in shear flow with application to lung aerosol dynamics—a review. *Journal of Biomechanical Engineering, 135*(2), Article 021008.
Kleinstreuer, C., & Zhang, Z. (2010). Airflow and particle transport in the human respiratory system. *Annual Review of Fluid Mechanics, 42*, 301–334.
Kolanjiyil, A. V., & Kleinstreuer, C. (2013a). Nanoparticle mass transfer from lung airways to systemic regions—Part I: Whole-lung aerosol dynamics. *Journal of Biomechanical Engineering, 135*(12), 11.
Kolanjiyil, A. V., & Kleinstreuer, C. (2013). Nanoparticle mass transfer from lung airways to systemic regions—Part II: Multi-compartmental modeling. *Journal of Biomechanical Engineering, 135*, Article 121004.
Kolanjiyil, A. V., & Kleinstreuer, C. (2016a). Computationally effecient analysis of particle transport and deposition in a human whole-airway model. Part I: Theory and model validation. *Computers in Biology and Medicine, 76*, 193–204.
Kolanjiyil, A. V., & Kleinstreuer, C. (2016b). Computationally efficient analysis of particle transport and deposition in a human whole-lung-airway model. Part I: Theory and model validation. *Computers in Biology and Medicine, 79*, 193–204.
Kolanjiyil, A. V., & Kleinstreuer, C. (2017). Computational analysis of aerosol-dynamics in a human whole-lung airway model. *Journal of Aerosol Science, 114*, 301–316.

Koullapis, P. G., Hofemeier, P., Sznitman, J., & Kassinosa, S. C. (2018b). An efficient computational fluid-particle dynamics method to predict deposition in a simplified approximation of the deep lung. *European Journal of Pharmaceutical Sciences, 113*, 132–144.
Kolanjiyil, A. V., Kleinstreuer, C., & Sadikot, R. T. (2017). Computationally efficient analysis of particle transport and deposition in a human whole-lung-airway model. Part II: Dry powder inhaler application. *Computers in Biology and Medicine, 84*, 247–253.
Koullapis, P., Kassinos, S. C., Muela, J., Perez-Segarra, C., Rigola, J., Lehmkuhl, O., & Nicolaou, L. (2018a). Regional aerosol deposition in the human airways: The SimInhale benchmark case and a critical assessment of in silico methods. *European Journal of Pharmaceutical Sciences, 113*, 77–94.
Koullapis, P. G., Nicolaou, L., & Kassinos, S. C. (2018). In silico assessment of mouth-throat effects on regional deposition in the upper tracheobronchial airways. *Journal of Aerosol Science, 117*, 164–188.
Koullapis, P. G., Nicolaou, L., & Kassinos, S. C. (2018). In silico assessment of mouth-throat effects on regional deposition in the upper tracheobronchial airways. *Journal of Aerosol Science, 117*, 164–188.
Kuga, K., Ito, K., Chen, W., Wang, P., & Kumagai, K. (2020). A numerical investigation of the potential effects of e-cigarette smoking on local tissue dosimetry and the deterioration of indoor air quality. *Indoor Air, 30*(5), 1018–1038.
Kuga, K., Ito, K., Yoo, S.-J., Chen, W., Wang, P., Liao, J., … Kumagai, K. (2018). First-and second-hand smoke dispersion analysis from e-cigarettes using a computer-simulated person with a respiratory tract model. *Indoor and Built Environment, 27*(7), 898–916.
Kwok, P. C. L., McDonnell, A., Tang, P., Knight, C., McKay, E., Butler, S. P., & Browne, E. (2020). In vivo deposition study of a new generation nebuliser utilising hybrid resonant acoustic (HYDRA) technology. *International Journal of Pharmaceutics, 580*, Article 119196.
Lambert, A. R., O'Shaughnessy, P. T., Tawhai, M. H., Hoffman, E. A., & Lin, C.-L. (2011). Regional deposition of particles in an image-based airway model: Large-eddy simulation and left-right lung ventilation asymmetry. *Aerosol Science and Technology, 45*(1), 11–25.
Levy, R., Hill, D. B., Forest, M. G., & Grotberg, J. B. (2014). Pulmonary fluid flow challenges for experimental and mathematical modeling. *Integrative and Comparative Biology, 54*(6), 985–1000.
Li, A., & Ahmadi, G. (1993). Deposition of aerosols on surfaces in a turbulent channel flow. *International Journal of Engineering Science, 31*(3), 435–451.
Lieber, B. B., & Zhao, Y. (1998). Oscillatory flow in a symmetric bifurcation airway model. *Annals of Biomedical Engineering, 26*(5), 821–830.
Lilly, D. K. (1992). A proposed modification of the Germano subgrid-scale closure method. *Physics of Fluids A: Fluid Dynamics, 4*(3), 633–635.
Lin, C. L., Tawhai, M. H., & Hoffman, E. A. (2013). Multiscale image-based modeling and simulation of gas flow and particle transport in the human lungs. *Wiley Interdisciplinary Reviews: Systems Biology and Medicine, 5*(5), 643–655.
Li, X., Shang, Y., Yan, Y., Yang, L., & Tu, J. (2018). Modelling of evaporation of cough droplets in inhomogeneous humidity fields using the multi-component Eulerian-Lagrangian approach. *Building and Environment, 128*, 68–76.
Longest, P. W., & Oldham, M. J. (2006). Mutual enhancements of CFD modeling and experimental data: A case study of 1-μm particle deposition in a branching airway model. *Inhalation Toxicology, 18*(10), 761–771.
Longest, P. W., Tian, G., Delvadia, R., & Hindle, M. (2012). Development of a stochastic individual path (SIP) model for predicting the deposition of pharmaceutical aerosols: Effects of turbulence, polydisperse aerosol size, and evaluation of multiple lung lobes. *Aerosol Science and Technology, 46*(12), 1271–1285.
Longest, P. W., Tian, G., Khajeh-Hosseini-Dalasm, N., & Hindle, M. (2016). Validating whole-airway CFD predictions of DPI aerosol deposition at multiple flow rates. *Journal of Aerosol Medicine and Pulmonary Drug Delivery, 29*(6), 461–481.
Malvè, M., Pérez del Palomar, A., Chandra, S., López-Villalobos, J., Mena, A., Finol, E., … Doblaré, M. (2011). FSI analysis of a healthy and a stenotic human trachea under impedance-based boundary conditions. *Journal of Biomechanical Engineering, 133*(2).
Mason, P. J. (1994). Large-eddy simulation: A critical review of the technique. *Quarterly Journal of the Royal Meteorological Society, 120*(515), 1–26.
McLellan, T., George, P. M., Ford, P., De Backer, J., Van Holsbeke, C., Mignot, B., … Thillai, M. (2020). Idiopathic pulmonary fibrosis: Airway volume measurement identifies progressive disease on computed tomography scans. *ERJ Open Research, 6*(1).
Menter, F. R. (1994). Two-equation eddy-viscosity turbulence models for engineering applications. *AIAA Journal, 32*(8), 1598–1605.
Menter, Langtry, R., & Völker, S. (2006). Transition modelling for general purpose CFD codes. *Flow, Turbulence and Combustion, 77*(1), 277–303.
Menter, F. R., Matyushenko, A., & Lechner, R. (2018). Development of a generalized K-ω two-equation turbulence model. In *Paper presented at the Symposium der Deutsche Gesellschaft für Luft-und Raumfahrt*.
Michaelides, E. E. (2003). Hydrodynamic force and heat/mass transfer from particles, bubbles, and drops—the Freeman scholar lecture. *Journal of Fluids Engineering, 125*(2), 209–238.
Myers, J. (2017). *Computational fluid dynamics in a terminal alveolated bronchiole duct with expanding walls: Proof-of-Concept in OpenFOAM*.
Nagels, M. A., & Cater, J. E. (2009). Large eddy simulation of high frequency oscillating flow in an asymmetric branching airway model. *Medical Engineering & Physics, 31*(9), 1148–1153.
NBIA, N. B. I. A. (2019). National biomedical imaging archive (NBIA). Retrieved from https://imaging.nci.nih.gov/ncia/login.jsf.
Nicoud, F., & Ducros, F. (1999). Subgrid-scale stress modelling based on the square of the velocity gradient tensor. *Flow, Turbulence and Combustion, 62*(3), 183–200.
Nijdam, J. J. (2013). Mesh and time-step independent computational fluid dynamics (CFD) solutions. *Chemical Engineering Education, 47*(4), 191–196.
Norouzi, H. R., Zarghami, R., Sotudeh-Gharebagh, R., & Mostoufi, N. (2016). *Coupled CFD-DEM modeling: Formulation, implementation and application to multiphase flows*. John Wiley & Sons.
Oakes, J. M., Marsden, A. L., Grandmont, C., Shadden, S. C., Darquenne, C., & Vignon-Clementel, I. E. (2014). Airflow and particle deposition simulations in health and emphysema: From in vivo to in silico animal experiments. *Annals of Biomedical Engineering, 42*(4), 899–914.
Oakes, J. M., Shadden, S. C., Grandmont, C., & Vignon-Clementel, I. E. (2017). Aerosol transport throughout inspiration and expiration in the pulmonary airways. *International Journal for Numerical Methods in Biomedical Engineering, 33*(9), e2847.
Pandal-Blanco, A., Barrio-Perotti, R., Agujetas-Ortiz, R., & Fernandez-Tena, A. (2019a). Implementation of a specific boundary condition for a simplified symmetric single-path CFD lung model with OpenFOAM. *Biomechanics and Modeling in Mechanobiology*, 1–13.
Paoletti, S. (2002). Polyhedral mesh optimization using the interpolation tensor. In *Paper presented at the IMR*.
Paz, C., Suarez, E., Vence, J., & Cabarcos, A. (2019). Analysis of the volume of fluid (VOF) method for the simulation of the mucus clearance process with CFD. *Computer Methods in Biomechanics and Biomedical Engineering, 22*(5), 547–566.
Perun, M. L., & Gaver, D., III (1995). Interaction between airway lining fluid forces and parenchymal tethering during pulmonary airway reopening. *Journal of Applied Physiology, 79*(5), 1717–1728.
Perun, M. L., & Gaver, D. P., III (1995b). *An experimental model investigation of the opening of a collapsed untethered pulmonary airway*.
Plathow, C., Ley, S., Fink, C., Puderbach, M., Heilmann, M., Zuna, I., et al. (2004). Evaluation of chest motion and volumetry during the breathing cycle by dynamic MRI in healthy subjects: Comparison with pulmonary function tests. *Investigative Radiology, 39*(4), 202–209.
Pletcher, R. H., Tannehill, J. C., & Anderson, D. (2012). *Computational fluid mechanics and heat transfer*. CRC press.
Rajendran, R. R., & Banerjee, A. (2019). Mucus transport and distribution by steady expiration in an idealized airway geometry. *Medical Engineering & Physics, 66*, 26–39. https://doi.org/10.1016/j.medengphy.2019.02.006
Reynisson, P. J., Scali, M., Smistad, E., Hofstad, E. F., Leira, H. O., Lindseth, F., & Langø, T. (2015). Airway segmentation and centerline extraction from thoracic CT–comparison of a new method to state of the art commercialized methods. *PloS One, 10*(12), Article e0144282.
Rigas, M. L., Catlin, S. N., Ben-Jebria, A., & Ultman, J. S. (2000). Ozone uptake in the intact human respiratory tract: Relationship between inhaled dose and actual dose. *Journal of Applied Physiology, 88*(6), 2015–2022.
Robinson, R. J., Snyder, P., & Oldham, M. J. (2007). Comparison of particle tracking algorithms in commercial CFD packages: Sedimentation and diffusion. *Inhalation Toxicology, 19*(6–7), 517–531.
Saffman, P. (1965). The lift on a small sphere in a slow shear flow. *Journal of Fluid Mechanics, 22*(2), 385–400.
Scans, C. C. (2020). COVID CT scans. Retrieved from http://www.covidctscans.org/.
Vaish, M., Kleinstreuer, C., Kolanjiyil, A. V., Saini, N., & Pillalamarri, N. R. (2016). Laminar/turbulent airflow and microsphere deposition in a patient-specific airway geometry using an open-source solver. *International Journal of Biomedical Engineering and Technology, 22*(2).

van der Schans, C. P., Postma, D. S., Koeter, G. H., & Rubin, B. K. (1999). Physiotherapy and bronchial mucus transport. *European Respiratory Journal, 13*(6), 1477–1486. https://doi.org/10.1034/j.1399-3003.1999.13f37.x
Scheinherr, A., Bailly, L., Boiron, O., Lagier, A., Legou, T., Pichelin, M., & Giovanni, A. (2015). Realistic glottal motion and airflow rate during human breathing. *Medical Engineering & Physics, 37*(9), 829–839.
Scheinherr, A., Bailly, L., Boiron, O., Legou, T., Giovanni, A., Caillibotte, G., et al. (2012). Glottal motion and its impact on the respiratory flow. *Computer Methods in Biomechanics and Biomedical Engineering, 15*(sup1), 69–71.
Schiller, C. F., Gebhart, J., Heyder, J., Rudolf, G., & Stahlhofen, W. (1988). *Deposition of monodisperse insoluble aerosol particles in the 0.005 to 0.2 μm size range within the human respiratory tract Inhaled Particles VI* (pp. 41–49). Elsevier.
Schroeter, J., Asgharian, B., & Kimbell, J. (2019). Mathematical modeling of inhaled therapeutic aerosol deposition in the respiratory tract. *Inhalation Aerosols: Physical and Biological Basis for Therapy, 1*, 41–55.
Seyfi Noferest, B., Santhanam, A. P., & Ilegbusi, O. J. (2018). Effect of gravity on subject-specific human lung deformation. *Mathematical and Computer Modelling of Dynamical Systems, 24*(1), 87–101.
Seyfi, B., Santhanam, A. P., & Ilegbusi, O. J. (2016). A biomechanical model of human lung deformation utilizing patient-specific elastic property. *Journal of Cancer Therapy, 7*(6), 402–415.
Shang, Y., Dong, J., Tian, L., Inthavong, K., & Tu, J. (2019). Detailed computational analysis of flow dynamics in an extended respiratory airway model. *Clinical Biomechanics, 61*, 105–111.
Shimazaki, Y., Okubo, M., Yamamoto, T., & Yoshida, A. (2009). Three-dimensional numerical simulation of nanoparticle inhalation and indoor pollution around breathing human. *Journal of Environment and Engineering, 4*(1), 145–161.
Silberberg, A. (1982). Rheology of mucus, mucociliary interaction, and ciliary activity. *Progress in Clinical & Biological Research, 80*, 25–28.
Smagorinsky, J. (1963). General circulation experiments with the primitive equations. *Monthly Weather Review, 91*(3), 99–164.
Smith, S., Cheng, Y.-S., & Yeh, H. C. (2001). Deposition of ultrafine particles in human tracheobronchial airways of adults and children. *Aerosol Science & Technology, 35*(3), 697–709.
Smith, D., Gaffney, E., & Blake, J. (2008). Modelling mucociliary clearance. *Respiratory Physiology & Neurobiology, 163*(1–3), 178–188.
Som, C., Wick, P., Krug, H., & Nowack, B. (2011). Environmental and health effects of nanomaterials in nanotextiles and facade coatings. *Environment International, 37*(6), 1131–1142.
Spagnolie, S. E. (2015). *Complex fluids in biological systems: Experiment, theory, and computation*. New York: Springer Science and Business Media.
Stahlhofen, W., Gebhart, J., & Heyder, J. (1981). Biological variability of regional deposition of aerosol particles in the human respiratory tract. *American Industrial Hygiene Association Journal, 42*(5), 348–352.
Stahlhofen, W., Rudolf, G., & James, A. (1989). Intercomparison of experimental regional aerosol deposition data. *Journal of Aerosol Medicine, 2*(3), 285–308.
Subramaniam, D. R., Mylavarapu, G., Fleck, R. J., Amin, R. S., Shott, S. R., & Gutmark, E. J. (2017). Effect of airflow and material models on tissue displacement for surgical planning of pharyngeal airways in pediatric down syndrome patients. *Journal of the mechanical behavior of biomedical materials, 71*, 122–135.
Su, W.-C., Chen, Y., Bezerra, M., & Wang, J. (2019). Respiratory deposition of ultrafine welding fume particles. *Journal of Occupational and Environmental Hygiene*, 1–13.
Sul, B., Altes, T., Ruppert, K., Qing, K., Hariprasad, D. S., Morris, M., & Wallqvist, A. (2019). Dynamics of the tracheal airway and its influences on respiratory airflows: An exemplar study. *Journal of Biomechanical Engineering, 141*(11), Article 111009.
Taherian, S., Rahai, H., Gomez, B. Z., & Waddington, T. (2014). Particulates depositions in patient-specific simulations of respiratory system. In *Paper presented at the ASME international mechanical engineering congress and exposition*.
Taherian, S., Rahai, H., & Waddington, T. (2011). CFD modeling and analysis of pulmonary airways/particles transport and deposition. In *Paper presented at the 41st AIAA fluid dynamics conference and exhibit*.
Talaat, K., & Xi, J. (2017). Computational modeling of aerosol transport, dispersion, and deposition in rhythmically expanding and contracting terminal alveoli. *Journal of Aerosol Science, 112*, 19–33.
Tawhai, M. H., Pullan, A. J., & Hunter, P. J. (2000). Generation of an anatomically based three-dimensional model of the conducting airways. *Annals of Biomedical Engineering, 28*, 793–802.
Tena, A. F., Fernandez, J., Alvarez, E., Casan, P., & Walters, D. K. (2016). Design of a numerical model of lung by means of a special boundary condition in the truncated branches. *Int J Numer Meth Biomed Engng, 33*(6), 1–9.
Thäter, G. (2016). Parallel dilute particulate flow simulations in the human nasal cavity. *Computers & Fluids, 124*, 197–207.
Tian, L., & Ahmadi, G. (2020). Computational modeling of fiber transport in human respiratory airways—a review. *Experimental and Computational Multiphase Flow, 3*, 1–20.
Tian, L., Ahmadi, G., Wang, Z., & Hopke, P. K. (2012). Transport and deposition of ellipsoidal fibers in low Reynolds number flows. *Journal of Aerosol Science, 45*, 1–18.
Tian, L., Inthavong, K., Lidén, G., Shang, Y., & Tu, J. (2016). Transport and deposition of welding fume agglomerates in a realistic human nasal airway. *Annals of Occupational Hygiene, 60*(6), 731–747.
Tu, J., Inthavong, K., & Ahmadi, G. (2012). *Computational fluid and particle dynamics in the human respiratory system*. Springer Science & Business Media.
Vreman, A. W. (2004). An eddy-viscosity subgrid-scale model for turbulent shear flow: Algebraic theory and applications. *Physics of Fluids, 16*(10), 3670–3681. https://doi.org/10.1063/1.1785131
Wall, W. A., & Rabczuk, T. (2008). Fluid–structure interaction in lower airways of CT-based lung geometries. *International Journal for Numerical Methods in Fluids, 57*(5), 653–675.
Wall, W. A., Wiechert, L., Comerford, A., & Rausch, S. (2010). Towards a comprehensive computational model for the respiratory system. *International Journal for Numerical Methods in Biomedical Engineering, 26*(7), 807–827.
Walters, D. K., & Luke, W. H. (2011). Computational fluid dynamics simulations of particle deposition in large-scale, multigenerational lung models. *Journal of Biomechanical Engineering, 133*(1), 011003.
Wang, Y., & Elghobashi, S. (2014). On locating the obstruction in the upper airway via numerical simulation. *Respiratory Physiology & Neurobiology, 193*, 1–10.
Wang, J., Xi, J., Han, P., Wongwiset, N., Pontius, J., & Dong, H. (2019). Computational analysis of a flapping uvula on aerodynamics and pharyngeal wall collapsibility in sleep apnea. *Journal of Biomechanics, 94*, 88–98.
Wei, X., Byron, P. R., & Longest, P. W. (2014). Predicting variations in lung dose with different mouth-throat models. In *Paper presented at the respiratory drug delivery*.
Werner, R., Ehrhardt, J., Schmidt, R., & Handels, H. (2008). Modeling respiratory lung motion: A biophysical approach using finite element methods. In *Paper presented at the medical imaging 2008: Physiology, function, and structure from medical images*.
West, J. B. (1979). *West's respiratory physiology: The essentials* (10th ed.).
Wilcox, D. C. (1998). *Turbulence modeling for CFD, 2*. CA: DCW industries La Canada.
Worth Longest, P., & Xi, J. (2008). Condensational growth may contribute to the enhanced deposition of cigarette smoke particles in the upper respiratory tract. *Aerosol Science and Technology, 42*(8), 579–602.
Wu, D., Miyawaki, S., Tawhai, M. H., Hoffman, E. A., & Lin, C.-L. (2015). A numerical study of water loss rate distributions in MDCT-based human airway models. *Annals of Biomedical Engineering, 43*(11), 2708–2721.
Xia, G., Tawhai, M. H., Hoffman, E. A., & Lin, C.-L. (2010). Airway wall stiffening increases peak wall shear stress: A fluid–structure interaction study in rigid and compliant airways. *Annals of Biomedical Engineering, 38*(5), 1836–1853.
Xi, J., Kim, J. W., & Si, X. A. (2016). Effects of nostril orientation on airflow dynamics, heat exchange, and particle depositions in human noses. *European Journal of Mechanics - B: Fluids, 55*, 215–228.
Xi, J., Kim, J., Si, X. A., Corley, R. A., Kabilan, S., & Wang, S. (2015b). CFD modeling and image analysis of exhaled aerosols due to a growing bronchial tumor: Towards non-invasive diagnosis and treatment of respiratory obstructive diseases. *Theranostics, 5*(5), 443–455.

Xi, J., & Longest, P. W. (2007). Transport and deposition of micro-aerosols in realistic and simplified models of the oral airway. *Annals of Biomedical Engineering, 35*(4), 560–581.
Xi, J., Talaat, K., & Si, X. A. (2018a). Deposition of bolus and continuously inhaled aerosols in rhythmically moving terminal alveoli. *The Journal of Computational Multiphase Flows, 10*(4), 178–193.
Xi, J., Wang, Z., Talaat, K., Glide-Hurst, C., & Dong, H. (2018b). Numerical study of dynamic glottis and tidal breathing on respiratory sounds in a human upper airway model. *Sleep and Breathing, 22*(2), 463–479.
Yang, Y. K., Kang, I. S., Hwang, J. H., & Park, J. C. (2017). CFD simulation for air-borne infection analysis in AII-room. *International Journal of Mechanical & Mechatronics Engineering, 11*(5), 1047–1052.
Yin, Y., Choi, J., Hoffman, E. A., Tawhai, M. H., & Lin, C.-L. (2010). Simulation of pulmonary air flow with a subject-specific boundary condition. *Journal of Biomechanics, 43*(11), 2159–2163.
Yin, Y., Hoffman, E. A., & Lin, C.-L. (2009). Local tissue-weight-based nonrigid registration of lung images with application to regional ventilation. In *Paper presented at the medical imaging 2009: Biomedical applications in molecular, structural, and functional imaging*.
Zhang, Y., Finlay, W. H., & Matida, E. (2004). Particle deposition measurements and numerical simulation in a highly idealized mouth–throat. *Journal of Aerosol Science, 35*(7), 789–803.
Zhang, Z., & Kleinstreuer, C. (2002). Transient airflow structures and particle transport in a sequentially branching lung airway model. *Physics of Fluids, 14*(2), 862–880.
Zhang, Z., Kleinstreuer, C., & Kim, C. S. (2008). Airflow and nanoparticle deposition in a 16-generation tracheobronchial airway model. *Annals of Biomedical Engineering, 36*(19), 2095–2110.
Zhang, L., & Li, Y. (2012). Dispersion of coughed droplets in a fully-occupied high-speed rail cabin. *Building and Environment, 47*, 58–66.
Zhao, J., Feng, Y., Bezerra, M., Wang, J., & Sperry, T. (2019). Numerical simulation of welding fume lung dosimetry. *Journal of Aerosol Science, 135*, 113–129.
Zhao, J. F., & Fromen, C. (2020). Glottis motion effects on the inhaled particle transport and deposition in a subject-specific mouth-to-trachea model: An CFPD study. *Computers in Biology and Medicine, 116*. Y.
Zhao, Y., & Lieber, B. B. (1994). *Steady expiratory flow in a model symmetric bifurcation*.
Zheng, Y. (2011). *Liquid plug dynamics in pulmonary airways*. UMI Dissertation Publishing.
Zhuang, Z., & Bradtmiller, B. (2005). Head-and-face anthropometric survey of US respirator users. *Journal of Occupational and Environmental Hygiene, 2*(11), 567–576.
Zhu, S., Kato, S., & Yang, J.-H. (2006). Study on transport characteristics of saliva droplets produced by coughing in a calm indoor environment. *Building and Environment, 41*(12), 1691–1702.
Zore, K., Caridi, D., & Lockley, I. (2020). *Fast and accurate Prediction of vehicle Aerodynamics using ANSYS mosaic mesh (0148-7191)*. Retrieved from.
Zore, K., Parkhi, G., Sasanapuri, B., & Varghese, A. (2019). Ansys mosaic poly-hexcore mesh for high-lift aircraft configuration. In *Paper presented at the 21th annual CFD symposium*.

Name: Yu Feng

Bio: Dr. Yu Feng is an Assistant Professor in the School of Chemical Engineering at Oklahoma State University. He is also a center investigator in the Oklahoma Center for Respiratory and Infectious Diseases (OCRID). Yu Feng was a Research Assistant Professor and Lab Manager of the Computational Multi-Physics Laboratory (CM-PL) at North Carolina State University. He has also held an affiliation with the DoD Biotechnology HPC Software Applications Institute (BHSAI) as a Research Scientist II. Dr. Feng's lab focuses on making contributions to the medical world and human life by providing well-posed solutions to patient-specific pulmonary health problems using multi-scale modeling techniques. He and his research team specialize in assessing the occupational exposure risks using computational fluid-particle dynamics (CFPD) models and Physiological based Toxicokinetic (PBTK) models spans over 10 years and has been summarized in more than 30 peer-reviewed journal papers and 40 conference proceedings. Dr. Feng is currently the Vice Chair of Health Related Aerosol Working Group in the American Association for Aerosol Research (AAAR).

Name: Jianan Zhao

Bio: Jianan Zhao is currently a Ph.D. student in the School of Chemical Engineering at Oklahoma State University. He earned his M.S. degree in Mechanical Engineering with an emphasis on computational fluid dynamics (CFD) from the University of Southern California in 2015. After two years working in the industry, he joined Oklahoma State University in Fall 2018 and is now a research assistant in the Computational Biofluidics and Biomechanics Laboratory (CBBL) under Dr. Yu Feng's supervision. His research focuses on developing efficient numerical tools to study aerosol transport in the patient-specific respiratory system and the development of an innovative, dynamic lung model.

Name: Hamideh Hayati

Bio: Hamideh Hayati pursued her Bachelor degree in Chemical Engineering from Bahonar University of Kerman, Kerman, Iran in 2014. During her final project on RAM-Related Calculation (Reliability, Availability, and Maintainability) of the Equipment of an Industrial Unit in Ilam, Iran, she realized her inclination towards computation modeling. She earned her M.S. degree in the same university, and worked on Modeling of Particle Deposition in Turbulent Flow on Wavy Plate and presented results showing that the wavy duct walls significantly increase the particle deposition rate. She was inspired by her M.S. thesis and determined to continue the computational fluid dynamics research in pulmonary respiratory systems. She joined Oklahoma State University in Fall 2018 and is now a Ph.D. student in the Computational Biofluidics and Biomechanics Laboratory (CBBL) under Dr. Yu Feng's supervision.

Name: Ted Sperry

Bio: Ted Sperry pursued the CBBL during undergraduate studies in Chemical Engineering at Oklahoma State University, and continued research with the lab as a graduate student. Modeling aspects of the natural world along with CFD have been areas of personal interest outside of the lab. Studying engineering to eventually help improve medicine has been a way to align those interests with a desire to enhance the quality of life on a large scale. CFD simulation of particle deposition in human airways has been his primary research focus up to this point. Drug delivery and PBPK modeling improvements are the future endpoints targeted by his research efforts as a Ph.D. student.

Name: Hang Yi

Bio: Hang Yi is a Ph.D. student focusing on LPG pool fire models and lung aerosol dynamics in CBBL lab advised by Dr. Yu Feng in the School of Chemical Engineering at Oklahoma State University. He obtained a B.S. in Safety Engineering (2013) and an M.S. in Safety Science and Engineering (2016) at Northeastern University (NEU), Shenyang, China.